Journal of Materials Chemistry A

ROYAL SOCIETY OF CHEMISTRY

REVIEW

View Article Online
View Journal | View Issue

Cite this: *J. Mater. Chem. A*, 2021, **9**, 2070

Interface engineering of transitional metal sulfide–MoS_2 heterostructure composites as effective electrocatalysts for water-splitting

Yanqiang Li, *[a] Zehao Yin,†[a] Ming Cui,[a] Xuan Liu,[a] Jiabin Xiong,[b] Siru Chen†*[b] and Tingli Ma *[cd]

Benefiting from the high electrochemical surface area brought by the 2D nanosheet structure, MoS_2 has received great research attention for the hydrogen evolution reaction (HER). Recently, it has been demonstrated that by constructing a transitional metal sulfide–MoS_2 heterostructure, the HER performance of the MoS_2-based catalysts can be further improved. It is even possible to obtain bifunctional catalysts for both HER and oxygen evolution reaction (OER) due to the synergistic effect of the different components in the composite, the electronic effect to enable an efficient electron transfer and appropriate binding energy for the intermediates of the electrocatalytic reactions, and the surface defects on the interface of the heterostructures. Herein, we review the recent progress on the construction of the transitional metal sulfide–MoS_2 heterostructure for water splitting based on non-self-supporting and self-supporting catalysts. The surface and interface parameters of the heterostructures are discussed in detail to reveal the key roles of the hybrid structures for energy conversion. We also pay special attention to the theoretical simulations based on first principles to clarify the relationships between the electrochemical performance and structure parameters. Finally, the prospects and challenges of the transition metal sulfide–MoS_2 heterostructures for water splitting in the future are proposed to prompt the reasonable design of transition metal sulfide–MoS_2 heterostructures for full water splitting.

Received 5th November 2020
Accepted 26th November 2020

DOI: 10.1039/d0ta10815d

rsc.li/materials-a

[a]*State Key Laboratory of Fine Chemicals, School of Petroleum and Chemical Engineering, Dalian University of Technology, Panjin Campus, Panjin 124221, China. E-mail: yanqiangli@dlut.edu.cn*

[b]*Center for Advanced Materials Research, Zhongyuan University of Technology, Zhengzhou, 450007, China. E-mail: siruchen@zut.edu.cn*

[c]*Department of Materials Science and Engineering, China Jiliang University, Hangzhou, 310018, China. E-mail: tinglima123@cjlu.edu.cn*

[d]*Graduate School of Life Science and Systems Engineering, Kyushu Institute of Technology, Kitakyushu, Fukuoka, 808-0196, Japan. E-mail: tinglima@life.kyutech.ac.jp*

† These authors contributed equally to this work.

Dr Yanqiang Li received his PhD degree at Jilin University in 2015. Then, he joined Dalian University of Technology as a lecturer. His research focuses on the design and preparation of functional materials and catalysts for electrochemical energy storage and conversion based on the combination of theoretical studies and electrochemical experiments.

Zehao Yin is a Master's degree candidate at Dalian University of Technology. He received her bachelor's degree from Xi'an University of Science and Technology. His research focuses on designing bifunctional electrocatalysts for high-performance zinc–air batteries.

1. Introduction

The ever-increasing energy demand and depletion of fossil energy promote research studies to explore clean and renewable energy sources.[1,2] Due to its carbon-free nature, hydrogen is considered an alternative clean energy carrier and has received widespread attention. However, there is no natural H_2 on Earth, and the hydrogen element exists in the form of compounds. As one of the most important H-containing compounds, water is the most extensive resource on the earth. According to calculations, if all of the hydrogen in seawater is extracted, the total heat generated by hydrogen is thousands of times higher than the heat released by all fossil fuels on the earth.[3–5] Therefore, the electrochemical splitting of water is a significant strategy to produce hydrogen. In addition, compared with the widely utilized methods to prepare hydrogen, such as steam reforming and coal gasification, the electrochemical electrolysis can produce purer hydrogen with no emission of greenhouse gases and other polluted gases.[6,7]

Electrochemical water splitting is a very mature technology, in theory, and two half reactions are involved: oxygen evolution reaction (OER) on the anode and hydrogen evolution reaction (HER) on the cathode.[8] The thermodynamic voltage for water splitting is 1.23 V at 25 °C and 1 atm.[9] However, in practical applications, a much larger potential is needed to drive this reaction due to the sluggish electrochemical kinetics. Nowadays, the energy conversion efficiency of water splitting is only 56–73%, and only less than 5% hydrogen is produced by this technology.[10] Therefore, it is necessary to develop efficient catalysts to accelerate the reaction rate of HER and OER. So far, Pt-based catalysts are demonstrated to be the most efficient HER catalysts,[11] while Ir and Ru oxides are regarded as the most efficient OER catalysts.[12] However, due to the scarcity and high price of precious metals on the earth, their large-scale commercial application is limited.[13] The development of catalysts with abundant earth reserves and excellent catalytic performance has become a critical factor in the commercialization of water splitting devices.

During the exploration process, transition metal-based compounds have been greatly investigated as electrocatalysts for efficient water splitting due to their earth-abundance and decent activity.[14–17] Among them, MoS_2 has received a lot of attention due to its high HER performance. MoS_2 shows a typical layered structure similar to graphene, with weak van der Waals interactions between adjacent S–Mo–S layers, where Mo atoms are sandwiched between sulfur atoms in a hexagonal arrangement.[18] The edge position of the MoS_2 layered structure has been proved by theoretical calculations to be the active site for HER. Its edge also has a large number of unsaturated S atoms, which has an adsorption free energy close to 0 for the intermediate product in the HER process, making H protons easily adsorbed and desorbed on the surface of MoS_2 to generate hydrogen.[19,20] When used as a HER catalyst, only a small overpotential is required for MoS_2 to achieve a higher current density. However, the surface layer of MoS_2 is considered to be inert, which makes the process of how to expose more edge sites a critical issue. In addition, the intrinsic conductivity of MoS_2 is relatively poor, which makes the resistance of the charge transport larger, resulting in larger potentials for the reaction.[21] Moreover, the poor OER performance of MoS_2 makes it unable to be used as a bifunctional catalyst to catalyze the water electrolysis.

At present, constructing metal sulfide–MoS_2 heterostructures through interface engineering has been demonstrated as one effective strategy to improve the catalytic performance of MoS_2-based catalysts.[22] Due to the different catalytic activities toward HER and OER of the different components in the composites, it is probable to obtain

Dr Siru Chen received her PhD degree at Jilin University in 2015. After three years research in Dalian Institute of Chemical Physics as a post-doctor, she joined Zhongyuan University of Technology as a lecturer in 2019. Her research focuses on the design and preparation of functional materials and catalysts for electrochemical energy storage and conversion.

Professor Tingli Ma received her PhD degree in 1999 from the Department of Chemistry, Faculty of Science of Kyushu University, Japan. She then joined the National Institute of Advanced Industrial Science and Technology (AIST) as a Post-doctoral Researcher from 1999 to 2004. She worked as a professor at the Dalian University of Technology, China from 2007 to 2018. She is currently working at the Graduate School of Life Science and Systems Engineering at Kyushu Institute of Technology, Japan and China Jiliang University. She leads research teams studying inorganic and organic solar cells, such as dyesensitized solar cells and perovskite solar cells, and other related projects, including development of catalysts, hydrogen production, functional dyes and nano-semiconductor materials.

bifunctional electrocatalysts for both OER and HER. In addition, heterostructures usually display increased electrocatalytic activities over the single-phase counterpart due to more exposed active sites on the interface, and the synergetic effect of the different components.[23] Moreover, the interaction between the various components will cause the redistribution of electrons at the heterogeneous interface, so that it has a moderate adsorption-free energy for H proton and O-containing intermediate, which is very beneficial for boosting the HER and OER performance of the composite.[24–27] Due to the rapid development of metal sulfide–MoS_2 heterostructures for water splitting, a review about interface engineering of the MoS_2-based electrocatalysts is necessary and meaningful to summarize the recent research progress on their design and application.

Table 1 Summary of non-self-supporting catalysts for HER, OER and water splitting

Electrocatalyst	Electrolyte	η @ j (mV @ mA cm^{-2})		Tafel slope (mV dec^{-1})		Overall voltage (V @ mA cm^{-2})	Stability	Ref.
		HER	OER	HER	OER			
Co_9S_8@MoS_2/CNFs	0.5 M H_2SO_4 for HER 1 M KOH for OER	190 @ 10	430 @ 10	110	61		Small changes in current density after 1000 CV cycles	47
Co_9S_8/NC@MoS_2	0.5 M H_2SO_4 for HER	117 @ 10		68.8			12 h @ 67 mV in 1 M KOH	51
	1.0 M PBS for HER	261 @ 10		126.1			12 h @ 117 mV in 0.5 M H_2SO_4	
	1 M KOH for HER	67 @ 10		60.3			12h @ 261 mV in 1.0 M PBS	
MCS-HP	0.5 M H_2SO_4 for HER	175 @ 10	410 @ 10 in 1 M KOH	55.6	90.1			53
	1 M KOH for HER	220 @ 10		115.3				
Co_9S_8/MoS_2@NSOC	0.5 M H_2SO_4 for HER	233 @ 10		96			With the loss of 11% and 9.4% respectively after 12 h work in the acidic and alkaline media	55
	1 M KOH for HER	194 @ 10		118				
CoS_2–C@MoS_2-25	0.5 M H_2SO_4 for HER 1 M KOH for OER	173 @ 10	391 @ 10	61	46		Current density remained virtually immobile for 1000 cycles	56
$CoS_{1.097}$/MoS_2	0.5 M H_2SO_4 for HER	228 @ 10		59			21 h @ 10 mA cm^{-2} in acidic, neutral and alkaline media for HER	57
	0.1 M PBS for HER	341 @ 10		85				
	1 M KOH for HER	249 @ 10		75				
Ni_9S_8@MoS_2	0.5 M H_2SO_4 for HER	88 @ 10		49			20 h @ 10 mA cm^{-2} for HER	64
NiS_2/MoS_2-RGO	0.5 M H_2SO_4 for HER	172 @ 10		51			10 h @ 10 mA cm^{-2} in 0.5 M H_2SO_4 and 1 M KOH for HER	68
	1.0 M PBS for HER	229 @ 10		103				
	1 M KOH for HER	144 @ 10		82				
MoS_2–NiS_2/NGF	1.0 M KOH	172 @ 10	370 @ 10	70		1.64 @ 10	24 h @ 10 mA cm^{-2}	73
CuS@defect-rich MoS_2	0.5 M H_2SO_4 for HER	135 @ 10		50			10 000 s @ 175 mV for HER	76
ZnS@C@MoS_2	1 M KOH for HER	118 @ 10		55.4			12 h @ 30 mA cm^{-2} for HER	80
MoS_2 NDs/VS_2	0.5 M H_2SO_4 for HER	291 @ 10		58.1			16 h @ 300 mV for HER	83
$NiCo_2S_4$@MoS_2	1 M KOH for HER	194 @ 10		62			10 h @ 10 mA cm^{-2} for HER	87
MoS_2/NiCoS	1 M KOH	189 @ 10	290 @ 10	75	77	1.50 @ 10	22 h @ 10 mA cm^{-2}	88
Co,Fe–MoS_2	1 M KOH	113 @ 10	264 @ 10	61	117	1.49 @ 10	10 h @ 10 mA cm^{-2}	89
MoS_2–g-$CuNi_2S_4$	0.5 M H_2SO_4 for HER	120 @ 10		29.3			Small changes in current density after 1000 CV cycles	90

Table 2 Summary of self-supporting catalysts for HER, OER and water splitting

Electrocatalyst	Electrolyte	Substrate	η @ j (mV @ mA cm^{-2})		Tafel slope (mV dec^{-1})		Overall voltage (V @ mA cm^{-2})	Stability	Ref.
			HER	OER	HER	OER			
$Co_5Mo_{10}S_x$/CC	1 M KOH	Carbon fiber cloth	36 @ 10	153 @ 10	56	58	1.51 @ 10	12 h @ 10 mA cm^{-2}	105
MoS_2/CoS_2	0.5 M H_2SO_4 for HER	Carbon fiber paper	126 @ 10	—	42.6	—	—	10 h @ 10 mA cm^{-2}	106
	1.0 M PBS for HER		196 @ 10		77.5				
	1 M KOH for HER		97 @ 10		78.7				
CoS_2/MoS_2 HNSAs	1 M KOH for HER	Ni foam	50 @ 10	—	76	—	—	70 h @ 100 mV	110
$CoMoS_x$/NF	1 M KOH	Ni foam	89 @ 10	345 @ 100	94	—	1.89 @ 500	25 h @ 500 mA cm^{-2}	113
Mo-doped Ni_3S_2	1 M KOH	Ni foam	212 @ 10	260 @ 10	98	85	1.67 @ 10	48 000 s @ 10 mA cm^{-2}	119
MoS_2–Ni_3S_2 HNRs/NF	1 M KOH	Ni foam	98 @ 10	290 @ 10	61	57	1.50 @ 10	48 h @ 17 mA cm^{-2}	120
MoS_2/Ni_3S_2 heterostructures	1 M KOH	Ni foam	110 @ 10	218 @ 10	83	88	1.56 @ 10	10 h @ 10 mA cm^{-2}	121
N–NiS/MoS_2	1 M KOH	Ni foam	71 @ 10	—	79	—	—	20 h @ 30 mA cm^{-2}	125
p-MoS_2/Ni_3S_2/NF	1 M KOH	Ni foam	99 @ 10	185 @ 10	71	46	—	35 h @ 10 mA cm^{-2}	128
MoS_2/FNS/FeNi foam	1 M KOH	FeNi foam	120 @ 10	204 @ 10	45.1	28.1	—	10 h @ 10 mA cm^{-2} for HER 10 h @ 204 mV for OER	134
(Ni, Fe)S_2@MoS_2	1 M KOH	Carbon fiber paper	130 @ 10	270 @ 10	101.2	43.2	1.56 @ 10	40 h @ 10 mA cm^{-2}	135
CoMoNiS–NF-31	1 M KOH	Ni foam	113 @ 10	166 @ 10	85	58	1.54 @ 10	24 h @ 20 mA cm^{-2} in 1 M KOH	138
	0.5 M H_2SO_4		103 @ 10	255 @ 10	55	78	1.45 @ 10	Decreased from 21.7 to 17.4 mA cm^{-2} after 80 min in 0.5 M H_2SO_4	
	1.0 M PBS		117 @ 10	405 @ 10	56	71	1.80 @ 10	20 h @ 1.80 V in 1.0 M PBS	
$Mo_{(1-x)}W_xS_2$@Ni_3S_2	1 M KOH	Ni foam	98 @ 10	285 @ 10	92	90	1.62 @ 10	50 h @ 10 mA cm^{-2}	139

In this review, we focus on the construction of transition metal sulfide–MoS_2 heterostructures as bifunctional electrocatalysts for overall water splitting. After the introduction on the background of the catalytic mechanism, the preparation process and structural characteristics of the materials are outlined based on non-self-supporting and self-supporting catalysts. The enhancement effects of the heterogeneous interfaces on the HER/OER performances of the catalysts are addressed, and the possible catalysis mechanism is discussed. Finally, the prospects and challenges of transition metal sulfide–MoS_2 heterostructures for water splitting in the future are proposed. It is anticipated that this review will promote the reasonable design of transition metal sulfide–MoS_2 heterostructures for full water splitting and other electrochemical energy conversion systems (Tables 1 and 2).

2. Mechanism for HER and OER

The HER reaction takes place at the cathode of the water electrolysis device, and mainly involves three reaction steps with two possible reaction mechanisms. One is the Volmer–Heyrovsky mechanism which contains the Volmer reaction and Heyrovsky reaction, and the other one is the Volmer–Tafel mechanism, which contains the Volmer reaction and Tafel reaction.[28] In both reaction mechanisms, the first step is the adsorption of H on the active sites (acidic medium) or the decomposition of a water molecule (alkaline medium) and adsorption of H to form adsorbed H, which is called the Volmer reaction or the discharge reaction. The second step is either the adsorbed H combines one proton/H_2O and an electron to form H_2 (Heyrovsky reaction), or two adsorbed H atoms combine to generate H_2 (Tafel reaction).[29]

Volmer reaction:

$$H_3O^+ + M + e^- \rightarrow M\text{–}H + H_2O \text{ (in acidic media)}$$

$$H_2O + M + e^- \rightarrow M\text{–}H + OH^- \text{ (in alkaline media)}$$

Heyrovsky reaction:

$$M\text{–}H + H_3O^+ + e^- \rightarrow M + H_2 + H_2O \text{ (in acidic media)}$$

$$M\text{–}H + H_2O + e^- \rightarrow H_2 + M + OH^- \text{ (in alkaline media)}$$

Tafel reaction:

$$2M\text{–}H \rightarrow 2M + H_2 \text{ (Tafel reaction in both acidic and alkaline media)}$$

Regardless of the different reaction mechanisms, the adsorbed H is always involved in the reactions, and the free energy of H adsorption is an important parameter to evaluate the intrinsic activity of an electrocatalyst for HER. When the adsorption of H on the surface of the catalyst is too weak, the Volmer reaction is the rate-determination step. Conversely, when the adsorption of H on the surface of the catalyst is too strong, the desorption of H_2 is the rate-determination step. Ideally, the free energy of H adsorption should be close to zero, like Pt.[30]

Compared with HER, OER (which occurs at the anode of the water electrolysis device) is a more complicated four-electron transfer process, and different intermediates (M–O, M–OH, M–OOH) are involved. The generally accepted reaction mechanisms in alkaline or acidic media are listed in the following equations. First, hydroxyl or water molecules are adsorbed on the catalyst to form M–OH. Then, M–OH continues to undergo an electron transfer to form M–O. After the formation of M–O, O_2 can be produced *via* two routes. One is the direct generation of molecular oxygen from two M–O species, and the other involves M–O being oxidized into the M–OOH species first, then O_2 is released from the M–OOH intermediate.[31–34]

In acidic media:

$$M + H_2O \rightarrow M\text{–}OH + H^+ + e^-$$

$$M\text{–}OH \rightarrow M\text{–}O + H^+ + e^-$$

$$2M\text{–}O \rightarrow 2M + O_2$$

$$M\text{–}O + H_2O \rightarrow M\text{–}OOH + H^+ + e^-$$

$$M\text{–}OOH \rightarrow M + O_2 + H^+ + e^-$$

In alkaline media:

$$M + OH^- \rightarrow M\text{–}OH + e^-$$

$$M\text{–}OH + OH^- \rightarrow M\text{–}O + H_2O + e^-$$

$$2M\text{–}O \rightarrow 2M + O_2$$

$$M\text{–}O + OH^- \rightarrow M\text{–}OOH + e^-$$

$$M\text{–}OOH + OH^- \rightarrow M + O_2 + H_2O + e^-$$

Like HER, OER involves the adsorption and desorption of oxygen-containing intermediates on the active sites.[35,36] When the adsorption of O on the surface of the catalyst is too weak, the M–OH species is not easily formed. In contrast, when the adsorption of O on the active sites is too strong, M–OOH and O_2 are not easy to generate. Therefore, the optimum of the adsorption free energy for the O-containing intermediates can be anticipated to enhance the OER performance of the catalysts.[37–39]

3. Heterostructure catalysts

3.1 Chemical synthetic strategy of transitional metal sulfide–MoS_2

The chemical synthetic strategies of transitional metal sulfide–MoS_2 heterostructure catalysts mainly fall into two types. One is the direct synthesis, where the metal sources and S sources are

dissolved in a solvent, followed by the solvothermal reaction. Based on whether the supports are added, self-supporting or nonself-supporting metal sulfide–MoS_2 heterostructures can be facilely synthesized. For example, using cobalt acetate and sodium molybdate as the Co and Mo sources, followed by the solvothermal reaction in the presence of thiourea, Cao and co-workers prepared Co_9S_8@MoS_2 hybrid nanospheres for overall water splitting.[40] Liu and co-workers prepared a self-supported MoS_2/Ni_3S_2 heterostructure catalyst by a facile one-step hydrothermal method, where sodium molybdate, Ni foam and thioacetamide were used as raw materials.[26]

The other type of synthesis strategy is a two-step reaction route, where bimetallic precursors are prepared first, and the sulfurization reaction was carried out subsequently to prepare the metal sulfides. The bimetallic precursors can be metal oxides, metal hydroxides or metal organic frameworks, and the sulfurization reaction can be a hydrothermal reaction or thermal annealing in the presence of sulfur sources. For example, using ZIF-67 as the precursor, Sun and co-workers prepared carbon supported Co_9S_8@MoS_2 hybrids by thermal annealing and sequenced solvothermal reaction.[41] By *in situ* growth of $Cu(OH)_2$ nanorod arrays on Co foam, and further hydrothermal reaction with sodium molybdate and thiourea, Yu and Co-workers prepared a Cu foam supported Cu_2S/MoS_2 heterostructure for HER.[42]

3.2 Features and advantages of heterostructure catalysts

Compared with single component catalysts, heterostructure catalysts that are composed of multicomponent have unique advantages. First, the synergistic effect occurred when a catalyst contains a multicomponent, and this can be fully utilized to develop bifunctional electrocatalysts by introducing H_2O/OH adsorption sites. A well-established viewpoint is that MoS_2 is very efficient for HER, and Co, Ni and Fe-based sulfides are beneficial for OER. Therefore, by forming heterostructure composites, the catalysts can be used for overall water splitting.

Second, the electronic effect is another factor that boosts the catalytic activity of heterostructure catalysts. This is because the strong electronic interaction between two different active components will efficiently reconstruct the active centers, which is favourable for yielding high catalytic activity. For example, Shao and co-workers observed electron transfer from (Ni, Fe)S_2 to MoS_2 in (Ni, Fe)S_2@MoS_2 heterostructures by X-ray photoelectron spectroscopy, and it is suggested that the electronic interaction between (Ni, Fe)S_2 and MoS_2 could weaken S–H_{ads} formed on the interface, which regulates H chemisorption to facilitate the Volmer–Heyrovsky process.[43] In other works, the roles of the electronic coupling effect were also observed, such as lowering the energy barrier of intermediates or achieving an appropriate binding energy for the electrocatalytic reactions.

Third, the defect effects are also observed in heterostructure catalysts. Introducing defects into the electrocatalysts is also an effective method to improve their catalytic performance. In heterostructure catalysts, the long-range orderly structures of the active species are interrupted due to the mismatch lattice arrangement; therefore, many defects can be formed. For example, Du and coworkers prepared a Co_9S_8/Ni_3S_2 heterostructure with a large number of lattice defects in the interface, and density functional theory indicates that the abundant lattice defects could boost the chemisorption of the intermediates, which greatly promoted its overall water splitting performance.[44]

3.3 Characterization of heterostructure catalysts

Accurately characterizing the interface interaction of heterostructure catalysts is crucial for designing and developing more efficient materials for catalysis. Generally, the various metal sulfide species and their crystal phases can be inferred from X-ray diffraction and transmission electron microscopy (TEM) techniques. In addition, high-resolution TEM images can be used to observe the intimate contact and the formed interfaces between different objects or phases. X-ray photoelectron spectroscopy (XPS) and ultraviolet photoemission spectroscopy can be utilized to characterize the electron interaction between the different species, and electron paramagnetic resonance (EPR) can be used to investigate the defects in the heterostructure catalysts. Combined with a more accurate theoretical model, the structures and interface interaction of heterostructure catalysts can be well established (Fig. 1 and 2).

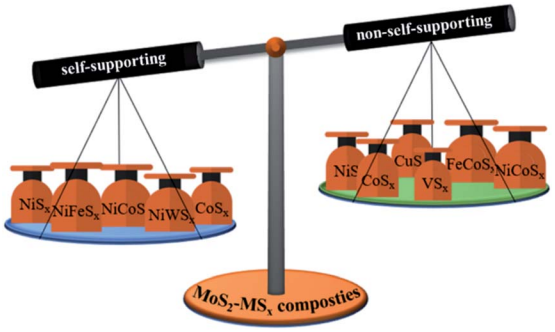

Fig. 1 A summary of various transition metal sulfide–MoS_2 heterostructure composites.

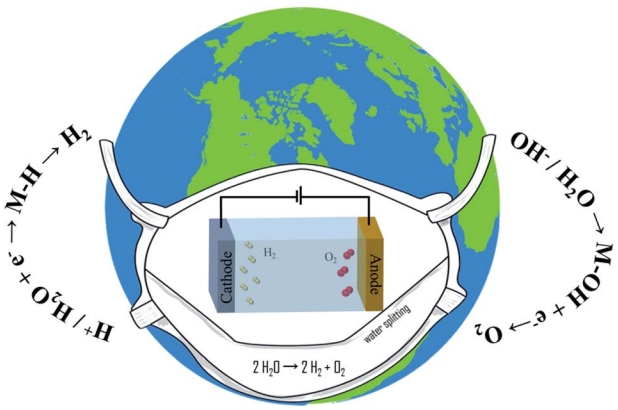

Fig. 2 Schematic diagram of the reaction mechanism for water splitting at the cathode (HER) and anode (OER).

4. Non self-supporting metal sulfide–MoS_2 heterostructure composites

4.1 CoS_x–MoS_2 heterostructure composites

Cobalt sulfides, including Co_9S_8, Co_3S_4, CoS_2 and CoS, have been demonstrated as attractive electrocatalysts for water splitting owing to their high catalytic activity, as well as excellent electrochemical stability for HER and OER.[45] When cobalt sulfides and MoS_2 are combined together to form reasonable and orderly heterostructures, the synergistic effect between the two components can enhance the overall electrochemical catalytic performance, which is better than the performance of each single component.[46] In 2015, using polyacrylonitrile (PAN) nanofibers with $Co(NO_3)_2$ and ammonium tetrathiomolybdate $(NH_4)_2MoS_4$ as the precursor, Zhu *et al.* synthesized a cubic cobalt sulfide-layered molybdenum disulfide core–shell/carbon nanofiber (Co_9S_8@MoS_2/CNFs) composite.[47] The Co_9S_8@MoS_2 core–shell nanostructure is composed of a Co_9S_8 nanoparticle core and fullerene-like MoS_2 shell. As shown in Fig. 3a and b, the authors investigated the HER pathways on the surface of MoS_2 and Co_9S_8@MoS_2 through first-principles calculations. Although the Co_9S_8@MoS_2 catalyst exhibits almost the same H atom adsorption energy compared with MoS_2, the chemical binding of the hydrogen molecules on the MoS_2 surface is much larger. Therefore, the desorption of H_2 from Co_9S_8@MoS_2 is easier, proving that by constructing the Co_9S_8/MoS_2 heterointerface, improved catalytic activity can be achieved due to the reduced energy barrier for the desorption of the H_2 molecule.

Recently, metal–organic frameworks (MOFs), which consist of metal ion nodes and organic linkers, have attracted increased attention due to their well-defined pore structure, high surface area, and tunable porosity.[48] Due to the weak coordination bonding and regular morphology of MOFs, they have been

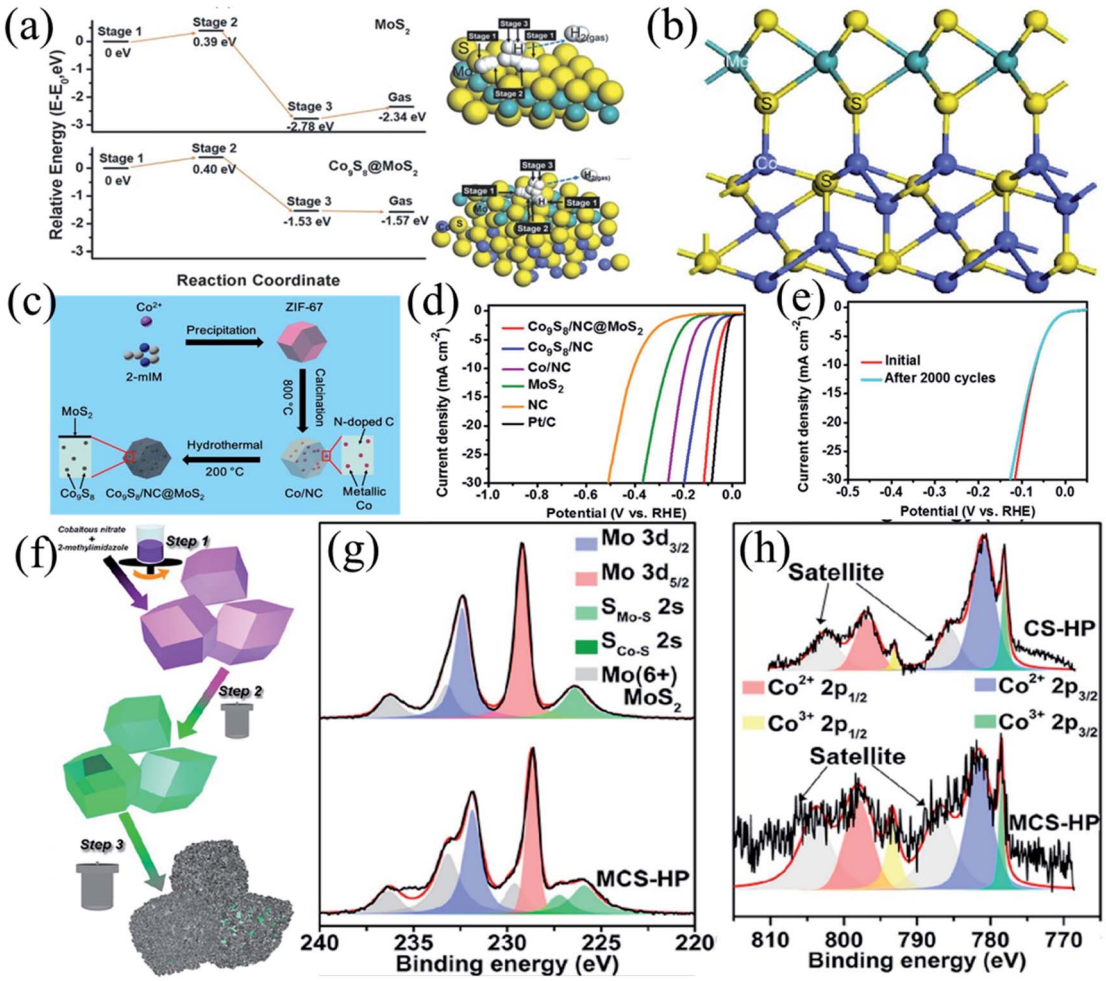

Fig. 3 (a) The kinetic energy barrier profiles of HER on the MoS_2 (top) and Co_9S_8@MoS_2 (down) catalysts. The right side shows the diffusion paths of H_2 on the MoS_2 and Co_9S_8@MoS_2 surfaces. (b) Optimized structures for the top view of H–MoS_2. Reproduced with permission.[47] Copyright 2015, Wiley-VCH. (c) Schematic illustration for the synthesis of Co_9S_8/NC@MoS_2 polyhedrons. (d) LSV curves of NC, Co/NC, MoS_2, Co_9S_8/NC, Co_9S_8/NC@MoS_2, and Pt/C in 1.0 M KOH and 0.5 M H_2SO_4. (e) Polarization curves of the Co_9S_8/NC@MoS_2 before and after 2000 CV cycles in 1.0 M KOH solution. Reproduced with permission.[51] Copyright 2017, American Chemistry Society. (f) Schematic illustration of the fabrication of MCS-HP. (g) Mo 3d and S spectra in MoS_2 and MCS-HP. (h) Co 2p in CS-HP, and MCS-HP. Reproduced with permission.[53] Copyright 2018, Elsevier.

widely utilized as good precursors for the synthesis of nanostructured electrode/catalyst materials.[49] As a well-known Co-based MOF, ZIF-67 has been widely investigated as a precursor for preparing Co-based catalysts.[50] Li *et al.* synthesized hierarchical porous Co_9S_8/N-doped carbon@MoS_2 (Co_9S_8/NC@MoS_2) polyhedrons for HER over a broad pH range by using ZIF-67 and ammonium molybdate as precursors (Fig. 3c).[51] Co_9S_8/NC@MoS_2 retains the polyhedral structure of ZIF-67, and the layered MoS_2 nanosheets are uniformly coated on the Co_9S_8/NC polyhedron. The Co/NC polyhedron derived by the carbonization of ZIF-67 has high porosity and active surface, which is beneficial for the nucleation and growth of MoS_2 nanosheets on the Co/NC polyhedron. The coupling interface between MoS_2 and the conductive carbon framework can reduce the work function of the carbon layers and optimize the electron structure, which is beneficial to accelerate the transfer of electrons. In addition, combining Co_9S_8 and MoS_2 into a reasonably designed structure can combine the inherent properties of these two materials together, enabling Co_9S_8/NC@MoS_2 with excellent HER activity over a broad pH range, with overpotentials of 67 at 10 mA cm^{-2} in 1.0 M KOH (Fig. 3d). In addition, the Co_9S_8/NC@MoS_2 electrode exhibits an overpotential increase of only 3 mV after 2000 CV cycles to afford a current density of 10 mA cm^{-2}, suggesting its good stability (Fig. 3e).

In addition to Co_9S_8/MoS_2 composite materials, ZIF-67 has been used as a precursor to prepare Co_3S_4/MoS_2 materials.[52] For example, using ZIF-67 and sodium molybdate as raw materials, Lei *et al.* synthesized a MoS_2/Co_3S_4 hollow polyhedral (MCS-HP) co-catalyst through the templated solvothermal method (Fig. 3f).[53] The synthesized MCS-HP exhibits a well-defined polyhedral structure with molybdenum sulfide nanosheets covering the surface of Co_3S_4. Through XPS characterization, it can be observed that the Mo and Co peaks have shifted. The MoS_2 that received electrons is in an electron-rich state, and the binding energy of Mo 3d is negatively shifted due to the shielding effect. On the contrary, due to the penetration effect, the Co 2p binding energy in the electron-deficient Co_3S_4 increased, demonstrating the strong interaction between MoS_2 and Co_3S_4 (Fig. 3g and h). By appropriately modifying the d orbital electrons of the transition metal sulfides, the electrochemical catalytic activity of the catalyst can be improved. It only needs overpotentials of 175 and 220 mV to achieve a current density of 10 mA cm^{-2} in acid and alkali media, respectively.

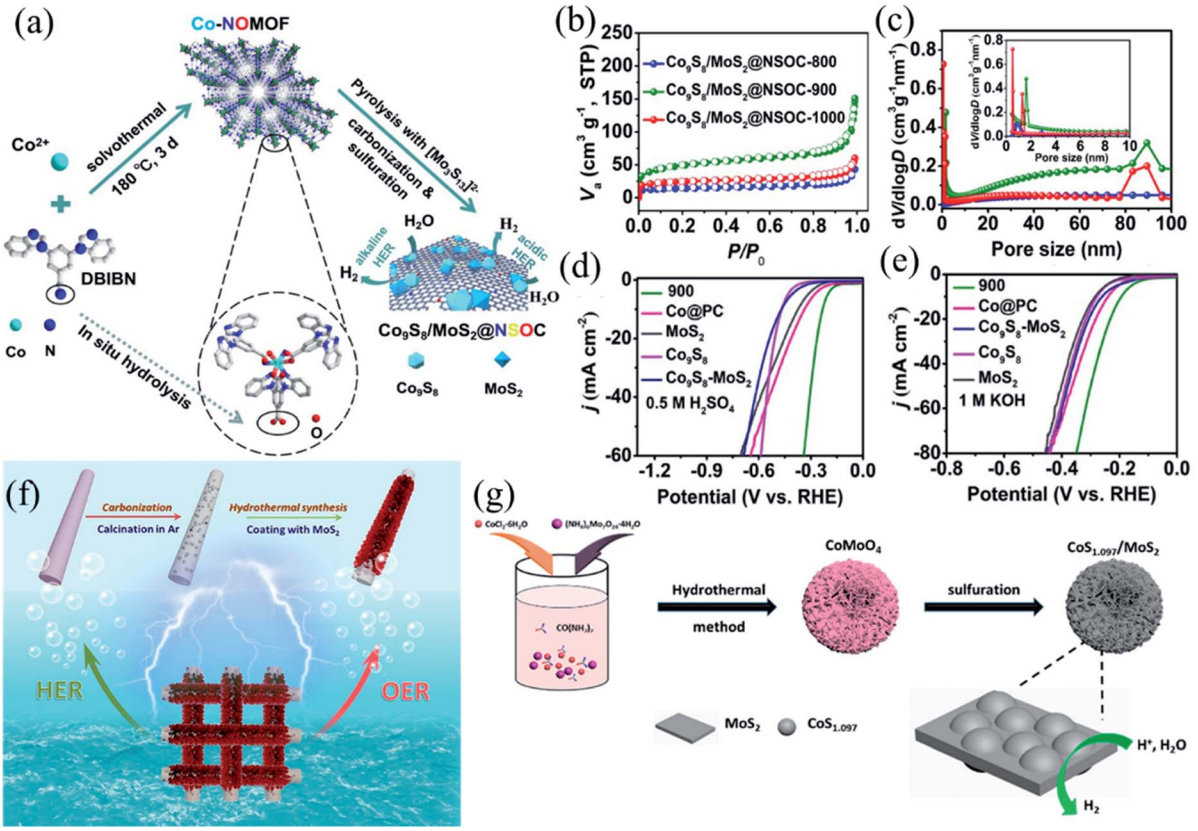

Fig. 4 (a) Schematic illustration for the synthesis of Co_9S_8/MoS_2@NSOC. (b) N_2 adsorption–desorption isotherms of Co_9S_8/MoS_2@NSOC. (c) Pore size distribution curves of the Co_9S_8/MoS_2@NSOC catalysts. (d and e) LSV curves of the Co_9S_8/MoS_2@NSOC900, Co@PC, MoS_2, Co_9S_8, Co_9S_8–MoS_2 materials for HER in 0.5 M H_2SO_4 and 1.0 M KOH solution. Reproduced with permission.[55] Copyright 2018, Royal Society of Chemistry. (f) Schematic illustration of the synthesis of CoS_2–C@MoS_2. Reproduced with permission.[56] Copyright 2019, American Chemistry Society. (g) Schematic illustration for the synthesis of $CoS_{1.097}$/MoS_2. Reproduced with permission.[57] Copyright 2019, American Chemistry Society.

In previous work, the MOF-templated synthesis of cobalt sulfide-based materials is limited due to the choice of ZIF-67 as the precursor, which requires an additional sulfurization process.[54] Recently, Chen prepared the bimetallic sulfide Co_9S_8/MoS_2 uniformly supported on N,S,O co-doped carbon (Co_9S_8/MoS_2@NSOC) through the one-step pyrolysis of the Co-based MOF (Co-NOMOF) with thiomolybdate $[Mo_3S_{13}]^{2-}$ (Fig. 4a).[55] The three-dimensional structure of Co-NOMOF facilitates the entry of Co nanoparticles into the carbon layer, and promotes the *in situ* doping of N and O atoms. Conversely, $[Mo_3S_{13}]^{2-}$ can introduce Mo and S sources, and further result in S doping into the carbon matrix. At the same time, it promotes the occurrence of the vulcanization process, and a Co_9S_8/MoS_2 heterogeneous was finally achieved. The porosity of the Co_9S_8/MoS_2@NSOC materials was investigated by N_2 adsorption at 77 K, and the results show that there are mesopores and micropores in Co_9S_8/MoS_2@NSOC. In addition, the calcination temperatures will significantly affect the pore structure of MOF-derived products. A high carbonization temperature is more beneficial to the formation of a porous structure. However, an excessively high temperature (1000 °C) will damage the porous structure, especially the mesopores to a certain extent (Fig. 4b and c). The rich pore structure can bring a large specific surface area to facilitate the transfer of electrolyte, and provide more active sites. Co_9S_8/MoS_2@NSOC-900 exhibited remarkable catalytic performance for HER with overpotentials of 194 and 233 mV in 1 M KOH and 0.5 M H_2SO_4 solution at 10 mA cm^{-2}, respectively, which is much better than the comparable catalysts, such as Co_9S_8, MoS_2 and Co_9S_8/MoS_2 (Fig. 4d and e). Its excellent performance can be ascribed to the unique electronic structure and lower local work function of the multi-heteroatom-doped carbon nanomaterials, the synergy between Co_9S_8 and MoS_2, and the Co_9S_8/MoS_2 heterogeneous interface that promotes the dissociation step of H_2O.

In addition to the MOF-templated synthesis strategy, other precursors were selected to synthesize cobalt–molybdenum bimetallic sulfides with regular morphologies. Through the one-step hydrothermal and vulcanization treatment of Co–C nanofibers, Zhu *et al.* synthesized hierarchical CoS_2–C@MoS_2 core–shell nanofibers (Fig. 4f).[56] The electrochemical measurements demonstrated that the conductivity and exposure of the active centers are two key factors that affect the catalytic performance of the catalyst. CoS_2–C makes up for the shortcomings of MoS_2 on conductivity, and has a synergistic effect with MoS_2 to improve the performance of the catalyst. Sun *et al.* used cobalt chloride and ammonium molybdate as raw materials to synthesize porous $CoS_{1.097}$/MoS_2 hybrid microspheres with rich defects through a one-step vulcanization (Fig. 4g).[57] Due to the synergy between $CoS_{1.097}$ and MoS_2, abundant defects and hierarchical interconnected microporous/mesoporous structure, the electrocatalytic activity of the $CoS_{1.097}$/MoS_2 hybrid microspheres show good HER performance, with overpotentials of 228, 249, and 341 mV at 10 mA cm^{-2} current density in 0.5 M H_2SO_4, 1 M KOH, and 0.1 M PBS electrolyte, respectively.

As shown above, for the synthesis of the CoS_x–MoS_2 heterostructure composites, direct hydrothermal reaction and MOFs templated method are usually utilized. For the direct hydrothermal reaction method, the obtained metal sulfides are usually sphere particles, which greatly restrict the exposure of active sites. Although hollow metal sulfides can be readily prepared by the MOFs templated strategy, it should be noted that the low yield and high cost of MOFs would prohibit the large-scale preparation of the composites. Therefore, a more effective synthetic strategy should be developed for the commercial application of the composites.

4.2 NiS_x–MoS_2 heterostructure composites

Nickel sulfides are considered to be highly efficient water electrolysis catalysts due to their excellent electrical conductivity.[58–60] However, the low density of the electrocatalytic sites on the surface and the low stability inhibit its further application.[61] Combining nickel sulfide with MoS_2 can produce a synergistic effect by constructing a heterogeneous interface and enrich the active sites, and great progress was achieved in this area.[62,63]

Using MoS_2 for the *in situ* growth of Ni_9S_8, Xu *et al.* prepared a Ni_9S_8@MoS_2 composite for HER.[64] Due to the electronic coupling between Ni_9S_8 and MoS_2, the charge transfer resistance for Ni_9S_8@MoS_2 is greatly reduced. The electrochemical surface area of Ni_9S_8@MoS_2 is also much larger than that for Ni_9S_8 and MoS_2, demonstrating the fast electron transfer and more exposed active sites of the Ni_9S_8@MoS_2 heterostructure (Fig. 5a–c). As a result, Ni_9S_8@MoS_2 exhibited good HER catalytic activity, with an overpotential of 88 mV at 10 mA cm^{-2} and a low Tafel slope of 49 mV dec^{-1}.

The catalytic efficiency of the catalyst is affected by its conductivity. Poor conductivity will cause additional overpotentials, which will consume more energy and reduce the apparent activity of the catalyst.[65–67] The combination of the MoS_2/NiS_x heterogeneous catalysts with high conductive carbon materials is expected to further improve the performance of the catalysts. Wang *et al.* synthesized a NiS_2/MoS_2 composite on reduced graphene oxide using $NiMoO_4$–RGO as the precursor,[68] and the tree-like NiS_2/MoS_2–RGO nanocomposites afford a current density of 10 mA cm^{-2} at small overpotentials of 172, 144 and 229 mV in acidic, alkaline and neutral solution, respectively. Xu *et al.* first treated graphene oxide with NH_3 to obtain the N-doped reduced graphene oxide, and then loaded Ni_3S_4/MoS_2 on the carbon support.[69] The optimized sample possesses a large number of catalytic active sites for HER and high conductive 3D networks that benefit electron transfer, and excellent catalytic activity was achieved.

Integrating 2D carbon materials with metal sulfides can improve the conductivity of the materials. However, due to the van der Waals interaction and strong π–π accumulation between the graphene layers, the 2D graphene is easy to aggregate. This irreversible aggregation not only hinders the uniform dispersion of the catalyst, but also makes the surface inaccessible to the reactants and electrolytes, which is not beneficial for the improvement of the catalytic performance.[70] In comparison, 3D graphene is an ideal scaffold for improving the electrocatalytic activity of the supported materials due to its high macroporosity

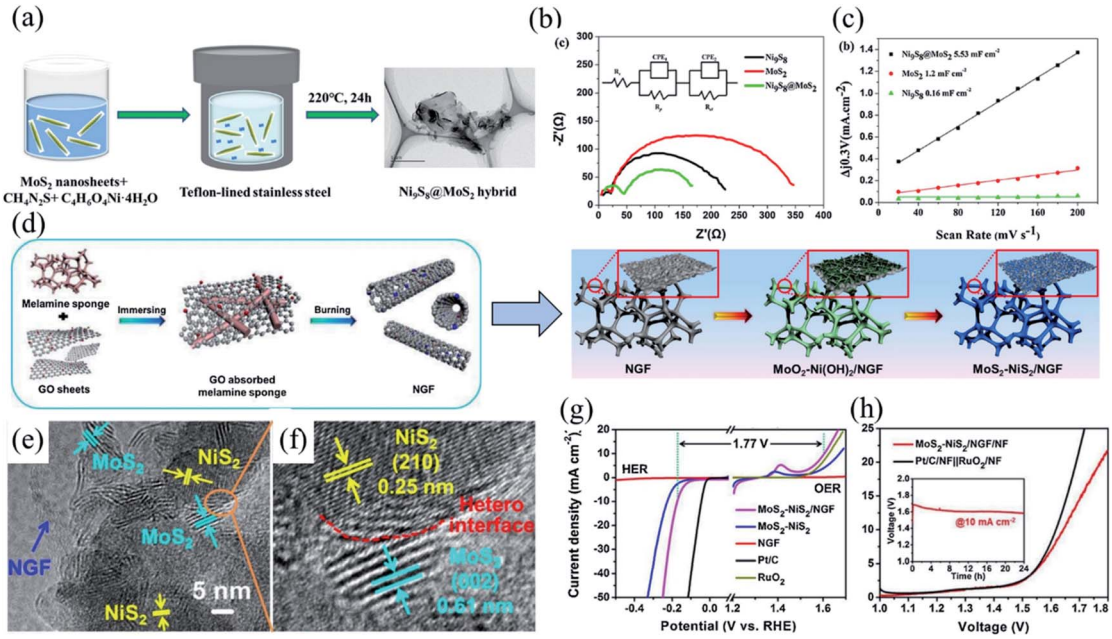

Fig. 5 (a) Schematic illustration of the heterostructure Ni_9S_8@MoS_2 hybrid. (b) EIS Nyquist plots of Ni_9S_8@MoS_2 and other materials. (c) Estimation of C_{dl} by plotting the current density variation *vs.* scan rate to fit a linear regression. Reproduced with permission.[64] Copyright 2019, Elsevier. (d) Schematic illustration for the formation of NGF and MoS_2–NiS_2/NGF. (e and f) HRTEM images of MoS_2–NiS_2/NGF. (g) Polarization curves of MoS_2–NiS_2/NGF, MoS_2–NiS_2, NGF, Pt/C, and RuO_2 in 1.0 M KOH for HER and OER. (h) Polarization curves of two-electrode overall water splitting using MoS_2–NiS_2/NGF/NF as both anode and cathode in 1.0 M KOH. Inset: galvanostatic measurement of the MoS_2–NiS_2/NGF/NF performed at a current density of 10 mA cm^{-2} in 1.0 M KOH. Reproduced with permission.[73] Copyright 2019, Elsevier.

and high conductivity.[71,72] Using melamine foam for the adsorption of graphene oxide and further burning off the melamine template, Kuang *et al.* first prepared a 3D interconnected macroscopic porous nitrogen-doped graphene foam (NGF).[73] The surface of the graphene foam with a negative charge can electrostatically adsorb Mo^{2+} and Ni^{2+} cations to form MoO_2–$Ni(OH)_2$ nanowalls on the NGF framework. Finally, after a CVD process, bimetallic sulfides of MoS_2–NiS_2 anchored on the 3D nitrogen-doped graphene foam (NGF) was successfully prepared and used as a bifunctional catalyst for water splitting (Fig. 5d). In comparison, the MoS_2–NiS_2 prepared without NGF exhibited severe agglomeration, which significantly reduced the contact area between the electrolyte and the catalyst, and hindered the release of gas products. The 3D hollow tube structure of MoS_2–NiS_2/NGF ensures abundant active sites and diverse paths to achieve the rapid and efficient transport of the electrolyte and gas. The TEM images clearly show that the heterointerface is formed between the (002) plane of MoS_2 and (210) plane of NiS_2 (Fig. 5e and f). In the electrolyte, H protons tend to be adsorbed by MoS_2, while OH tends to be adsorbed by NiS_2, resulting in the rapid dissociation step of H–O at the heterogeneous interface. The special catalyst delivered a current density of 10 mA cm^{-2} at overpotentials of 172 mV for HER and 370 mV for OER in 1.0 M KOH. Furthermore, when used in an alkaline water electrolyzer, MoS_2–NiS_2/NGF can produce the vigorous and continuous evolution of H_2 and O_2 at a current density of 10 mA cm^{-2} under a cell voltage of 1.64 V (Fig. 5g and h).

Although integrating carbon materials with metal sulfides could effectively improve the conductivity of the catalysts and prohibit the aggregation of MoS_2, it should be noted that the real charming fascinating of MoS_2 is its 2D nanosheet structure, which can expose the maximum number of active sites. Although it is possible to obtain several layers of MoS_2 by exfoliation technology, the preparation of the ultrathin MS_x–MoS_2 nanosheet is rarely reported. It is also very significant to synthesize the few-layers and even the single layer MS_x–MoS_2 heterostructure catalysts to boost their catalytic performances.

4.3 MS_x–MoS_2 (M = Cu, Zn, V) heterostructure composites

Due to its anisotropic properties, CuS can provide a penetration channel for ion adsorption and transmission.[74] Meanwhile, the S atom in CuS contains empty 3p orbitals and a large number of electrons, which has a strong tendency to capture electrons and promote electron transfer reactions with electron donor molecules.[75] Therefore, designing CuS and MoS_2 composites could facilitate electron transfer during the catalytic process. In addition, introducing defects into catalysts is a valid strategy to promote their catalytic activity. In a recent study, Liu *et al.* synthesized a CuS@defect-rich MoS_2 (CuS@MoS_2-DR) core–shell structure and investigated its catalytic activity for HER.[76] The CuS nanosphere was synthesized first, and SiO_2 was coated on the surface of CuS for the further growth of MoS_2 by using sodium molybdate and thiourea as raw materials. After removing SiO_2 by HF etching, CuS@MoS_2-DR was prepared. By changing the molar ratio of sodium molybdate and thiourea, the authors found that excess thiourea can be adsorbed on the surface of MoS_2 to hinder the growth of oriented crystals,

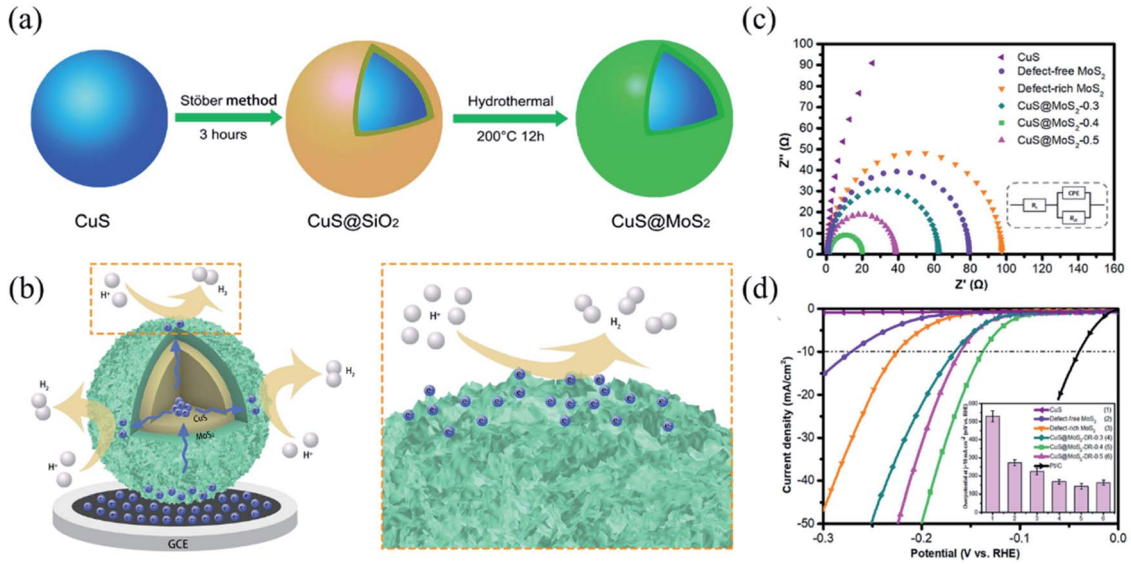

Fig. 6 (a) Schematic illustration for the synthesis of CuS@MoS_2. (b) Schematic illustration of the charge transfer in CuS@MoS_2-DR and the proposed mechanism for HER. (c) Nyquist plots of CuS@MoS_2-DR with other materials. (d) Polarization curves of CuS@MoS_2-DR with other materials. Reproduced with permission.[76] Copyright 2020, Elsevier.

thereby forming a defect structure with many dislocations, distortions and the cracking of the basal planes (Fig. 6a). In the HER catalysis process, CuS can effectively trap the excess electrons of defect-rich MoS_2, and then quickly transport them to the core–shell structure (Fig. 6b). Through EIS characterization, it can be found that the integration of CuS and MoS_2 can significantly reduce the charge transport resistance, and CuS@MoS_2-DR-0.4 with 40% MoS_2 loading has the best conductivity (Fig. 6c). Benefiting from the additional active edge sites of the defect-rich MoS_2 and the improved charge transport facilitated by the intimate interface, the CuS@defect-rich MoS_2 could afford a current density of 10 mA cm^{-2} at a low overpotential of 135 mV (Fig. 6d).

In addition to copper sulfide, transition metals ZnS have received extensive attention because of their excellent electrical conductivity for electrocatalysis.[77–79] Liu *et al.* synthesized hierarchical ZnS@C@MoS_2 core–shell nanostructures by the bottom-up two-step hydrothermal strategy combined selective etching method (Fig. 7a).[80] As the core, ZnS is covered with a defective porous carbon shell, and ultra-thin MoS_2 nanosheets are grown on the surface of the carbon shell. The coexistence of the ZnS semiconductor and the porous defect-rich carbon shell not only increases the conductivity of the material (Fig. 7b), but also separates and supports exfoliated MoS_2 nanosheets, which can effectively expose a large number of catalytically active edge sites. The hierarchical ZnS@C@MoS_2 core–shell nanostructures exhibited a low overpotential of 118 mV at 10 mA cm^{-2} for HER (Fig. 7c).

In addition, VS_2 has gradually become a kind of promising electrocatalyst due to its unique electronic structure. Unlike other

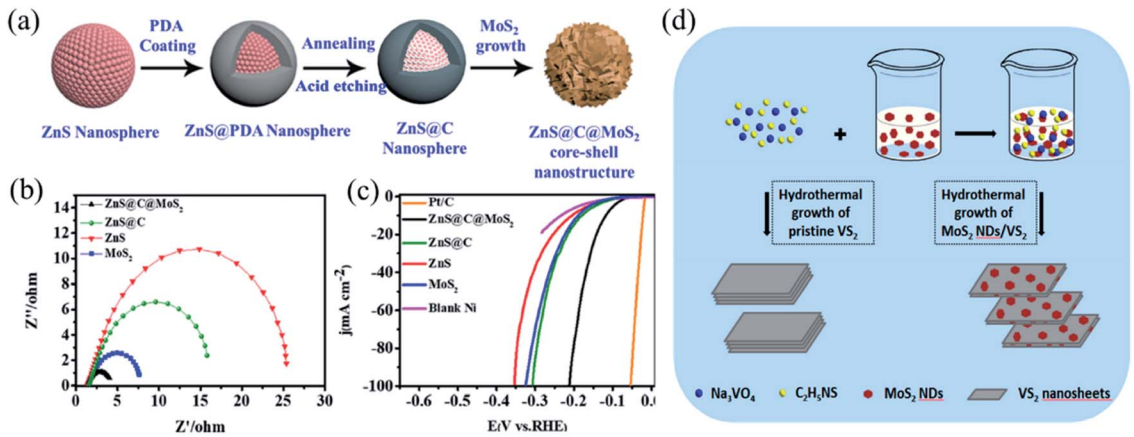

Fig. 7 (a) Schematic representation for the synthesis of ZnS@C@MoS_2. (b) Nyquist plots of ZnS@C@MoS_2 with other materials. (c) Polarization curves of ZnS@C@MoS_2 with other materials for HER in 1.0 M KOH. Reproduced with permission.[80] Copyright 2019, Elsevier. (d) Schematic illustration of the synthesis of MoS_2 NDs/VS_2 and pristine VS_2. Reproduced with permission.[83] Copyright 2018, American Chemistry Society.

transition metal sulfides, VS_2 shows an inherent metallic electronic ground state and unique electrical conductivity, making it a potential active HER electrocatalyst.[81,82] Du *et al.* synthesized a layered heterostructure composed of MoS_2 nanodots and metal VS_2 nanosheets by *in situ* hydrothermal using water-soluble monolayer MoS_2 nanodots as the size-controllable precursor, and sodium orthovanadate and thioacetamide as the sources of V and S, respectively.[83] During the hydrothermal process, MoS_2 nanodots act as a separator to inhibit the restacking of VS_2 nanodots, while layered VS_2 nanosheets act as a supporting skeleton to effectively hinder the agglomeration of MoS_2 nanodots (Fig. 7d). MoS_2 and VS_2 can form a highly lattice-matched electron transfer heterojunction due to the orbital interaction. The redistribution of the charge is beneficial to stabilizing VS_2, making it exhibit metallic characteristics and improve the overall conductivity. The optimized hybrid material exhibits significant electrocatalytic performance in acidic media due to its thinner flake heterostructure, higher conductivity, more catalytic active centers and higher intrinsic activity. Moreover, the LSV polarization curves before and after 1000 CV are almost the same, and the current density remains stable after 16 hours of chronoamperometry, demonstrating its good stability.

4.4 Non-self-supporting MoS_2-based trimetallic sulfide composites

Constructing a ternary metal sulfides–MoS_2 composite can further improve the catalytic activity of the multiple transition metal sulfides due to the more abundant interfaces and active sites.[84] The heterogeneous interface in multiple transition metal sulfides can increase the electron density at the active edge, and the electronic structure of the catalysts can be further optimized due to the synergistic effect of various metal sulfides.[85] Hu *et al.* designed $MoS_2/CoNi_2S_4$ composites based on the theory-calculation guidance.[86] By simultaneously modulating the 3d band offset of Ni, Co, and Mo near the interface, the author optimized the electronic structure of $MoS_2/CoNi_2S_4$. According to dual-pathway kinetic analyses, it can be found that under acid–base conditions, the activation energy of $MoS_2/CoNi_2S_4$ in both Heyrovsky and Volmer steps is slightly lower than that of the MoS_2 nanosheet (Fig. 8a and b), indicating that $MoS_2/CoNi_2S_4$ has better kinetics in acid and alkali media than MoS_2. The hybridization of MoS_2 and $CoNi_2S_4$ accelerates the dissociation step of water molecules induced by the charge transfer in an alkaline environment. DFT analysis showed that the electronic modulator Mo in $MoS_2/CoNi_2S_4$ simultaneously modified Ni and Co atoms, which not only activated Ni, but also alleviated the over-binding effect from Co (Fig. 8c–e). Due to the well-defined electronic structure of the $MoS_2/CoNi_2S_4$ composite, it could effectively adsorb H and OH in an alkaline environment to boost its overall water splitting performance.

Using ZIF-67 as template, Song *et al.* synthesized hollow core–shell $NiCo_2S_4$@MoS_2 polyhedrons, where MoS_2 nanosheets were assembled on $NiCo_2S_4$ nanobuilding blocks (Fig. 8f).[87] Compared with $NiCo_2S_4$ dodecahedrons, $NiCo_2S_4$@MoS_2 exhibits better HER performance under alkaline

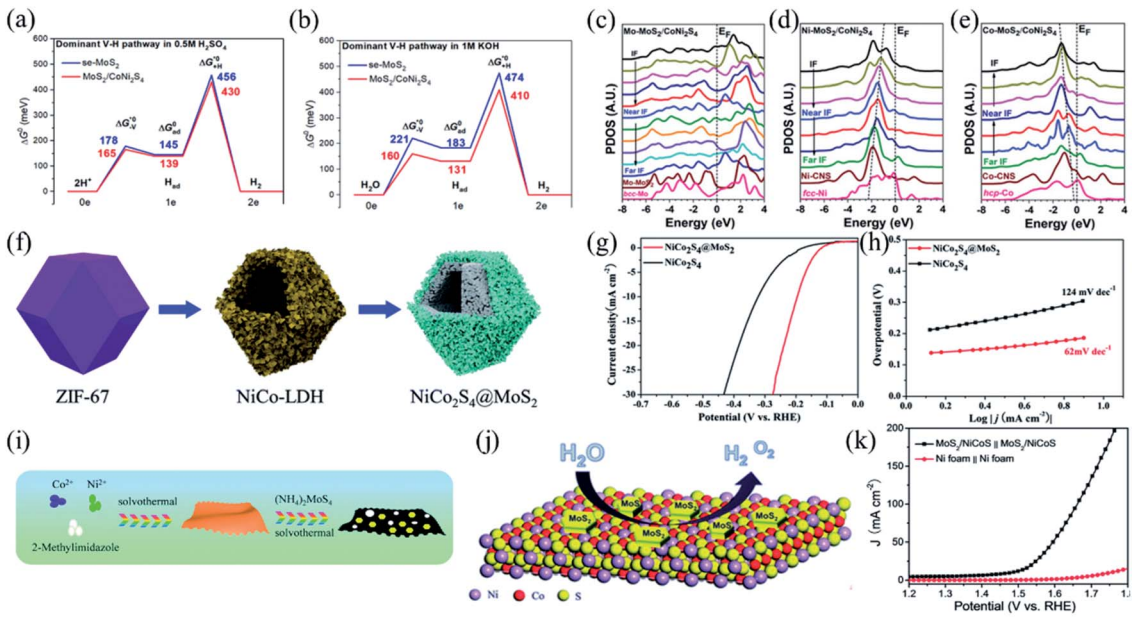

Fig. 8 (a and b) Comparison of the free energy diagram for the dominated Volmer–Heyrovsky pathways of MoS_2 and $MoS_2/CoNi_2S_4$ catalysts for HER in 0.5 M H_2SO_4 and 1 M KOH electrolytes, respectively. (c) The site-dependent PDOSs of Mo from the interface regions toward the metal Mo. (d) The site-dependent PDOSs of Ni from the interface toward metal Ni. CNS represents $CoNi_2S_4$ bulk. (e) The site-dependent PDOSs of Co from the IF regions toward the metal Co. Reproduced with permission.[86] Copyright 2019, Wiley-VCH. (f) Schematic illustration of the synthesis of $NiCo_2S_4$@MoS_2. (g and h) Polarization LSV curves and Tafel plots of $NiCo_2S_4$@MoS_2 and $NiCo_2S_4$ in 1 M KOH. Reproduced with permission.[87] Copyright 2019, Royal Society of Chemistry. (i) Schematic of the preparation of MoS_2/NiCoS heterostructures. (j) Schematic illustration of the water splitting process for MoS_2/NiCoS heterostructures. (k) Polarization curves for water splitting using MoS_2/NiCoS and Ni foam as bifunctional catalysts in a 1.0 M KOH solution. Reproduced with permission.[88] Copyright 2019, Royal Society of Chemistry.

conditions (Fig. 8g and h), indicating that the synergy between $NiCo_2S_4$ and MoS_2 is beneficial to increase the catalytic activity. Together with a 3D architecture of the outer MoS_2, the hollow structure prevents the adhesion of H_2 bubbles to the electrode surface, thereby keeping the integrity of the necessary solid–liquid interface. Qin *et al.* also synthesized MoS_2/NiCoS nanosheets and investigated their catalytic performance for water splitting through a MOF-templated strategy.[88] The authors synthesized NiCo–MOF nanosheets first, which then reacted with $(NH_4)_2MoS_4$ to generate two-dimensional porous MoS_2/NiCoS (Fig. 8i). The two-dimensional porous structure of MoS_2/NiCoS can expose more unsaturated S boundaries, therefore providing more active centers. At the same time, nanopores can promote the release of gas products and improve the stability of the catalyst. In addition, the multiple heterogeneous interfaces can modify the electronic structure of the catalyst, and the mixed-valence states of Ni, Mo, and Co further enhance the catalytic performance (Fig. 8j). The optimized MoS_2/NiCoS catalyst exhibited overpotentials of 189 mV for HER and 290 mV for OER at 10 mA cm^{-2} in 1 M KOH solution. In particular, the MoS_2/NiCoS catalyst only requires a voltage of 1.50 V to derive a current density of 10 mA cm^{-2} in a two-electrode electrolyzer (Fig. 8k).

Si *et al.* used $Co_3[Fe(CN)_6]_2$ nano cubes as self-sacrificing templates for the *in situ* growth of a MoS_2 nanosheet, during which process Co and Fe are successfully doped into MoS_2 (Fe, Co–MoS_2). The doping of Co and Fe not only create additional catalytic sites, but also could regulate the electronic structure of MoS_2.[89] The prepared catalyst retains the cubic geometric structure of the self-sacrificial template, and provides the comprehensive advantages of a high surface area, short charge transfer path, and easily accessible active sites. When used as bifunctional catalysts for water electrolysis, Co,Fe–MoS_2 shows excellent catalytic activity with a low cell potential of 1.49 V at a current density of 10 mA cm^{-2}. Adarakatti *et al.* synthesized a MoS_2/$CuNi_2S_4$ composite catalyst supported on graphene for HER.[90] By introducing transition metal (Cu and Ni) dopants, the adsorption affinity of the active edge to the intermediate hydrogen protons can be increased. Through detailed XPS analysis, it was proved that by anchoring the active center on the graphene framework, the exposure of the unsaturated S edge active sites can be increased, thereby significantly improving the intrinsic hydrogen evolution reaction activity of the MoS_2/$CuNi_2S_4$ nanosheets.

As illustrated above, nowadays, most of the MS_x–MoS_2 heterostructure composites focus on Co and Ni-based sulfides, probably due to the high OER activity of cobalt sulfides and nickel sulfides. However, it should be noted that from the viewpoint of commercial application, Fe and Mn-based sulfides are more promising due to their low toxicity and low cost. Therefore, more efforts should be devoted toward developing these potential catalysts.

5. Self-supporting catalysts

As stated above, non-self-supporting catalysts perform well at small current densities and short-term cycles. However, in industrial applications, high current densities and long working-life (such as thousands of hours) are required, and the performance of non-self-supporting catalysts is not satisfactory.[91] On the one hand, non-self-supporting catalysts require a polymeric binder to bond it on the working electrode.[92] This process inevitably reduces the electrochemically accessible specific surface area, and inhibits the mass and charge transfer rate in the electrochemical process.[93] On the other hand, due to the limited cohesive force of the binder, the electrocatalysts may peel off from the working electrode under high current densities,[94] resulting in unsatisfactory long-term stability.

Compared with conventional coating catalysts, self-supporting catalysts that are *in situ* grown on conductive substrates can effectively avoid these defects faced by non-self-supporting catalysts.[95] First, due to the strong adhesion of catalysts with the substrates, the self-supporting catalyst will not peel off even if it is cycled under high voltage for a long time. Second, the self-supporting catalysts are usually of nanowire, nanorod, nanosheet or nano bundle morphology, which can expose more active sites and facilitate gas release from its surface. Third, the conductive substrate can further speed up the charge transfer rate.[96–98] Therefore, the MoS_2-based self-supporting catalysts have attracted more wide research interests in recent years.[99,100]

5.1 Self-supporting CoS_x–MoS_2 composites

Benefiting from the existence of heterogeneous interfaces between MoS_2 with CoS_x and the excellent conductivity provided by conductive substrate, the designed MoS_2–CoS_x catalyst *in situ* grown on a conductive substrate can exhibit excellent bifunctional catalytic performance for HER and OER.[101–104] Lu *et al.* used the Evans–Showell-type polyoxometalate (POM) $Co_3[Co_2Mo_{10}O_{38}H_4]$ as the precursor to construct a CoS_2/MoS_2 heterogeneous interface through the precise engineering of CoMoS active sites at the atomic level (Fig. 9a).[105] The catalytic activity of CoMoS was investigated by density functional theory calculations (Fig. 9b and c). Compared with pure MoS_2, which has inferior activity for alkaline HER reaction with a high water dissociation energy barrier, the introduction of Co enables the water decomposition to proceed with a much lower potential energy barrier on the Co site and Co–S site of CoMoS. IN particular, the S site located on the Co edge shows an extremely optimized adsorption energy for both OH and H groups (−0.17 eV). That is, the CoS_2/MoS_2 heterogeneous interface can promote the HER activity in alkaline media by reducing the water dissociation energy barrier on the Co edge or S atom located at the Co edge.

Huang *et al.* also studied the heterogeneous interface effects between MoS_2 and CoS_2. The author synthesized a 3D MoS_2/CoS_2 composite with a shell/core heterostructure that was *in situ* grown on carbon fiber paper (Fig. 9d).[106] According to XPS and Raman analysis (Fig. 9e and f), compared with pure MoS_2 and CoS_2, the binding energy and Raman vibration peak of the MoS_2 phase in MoS_2/CoS_2 composites shifted negatively, while the binding energy and the Raman vibration peak of the CoS_2 phase shifted positively, demonstrating the electron transfer from

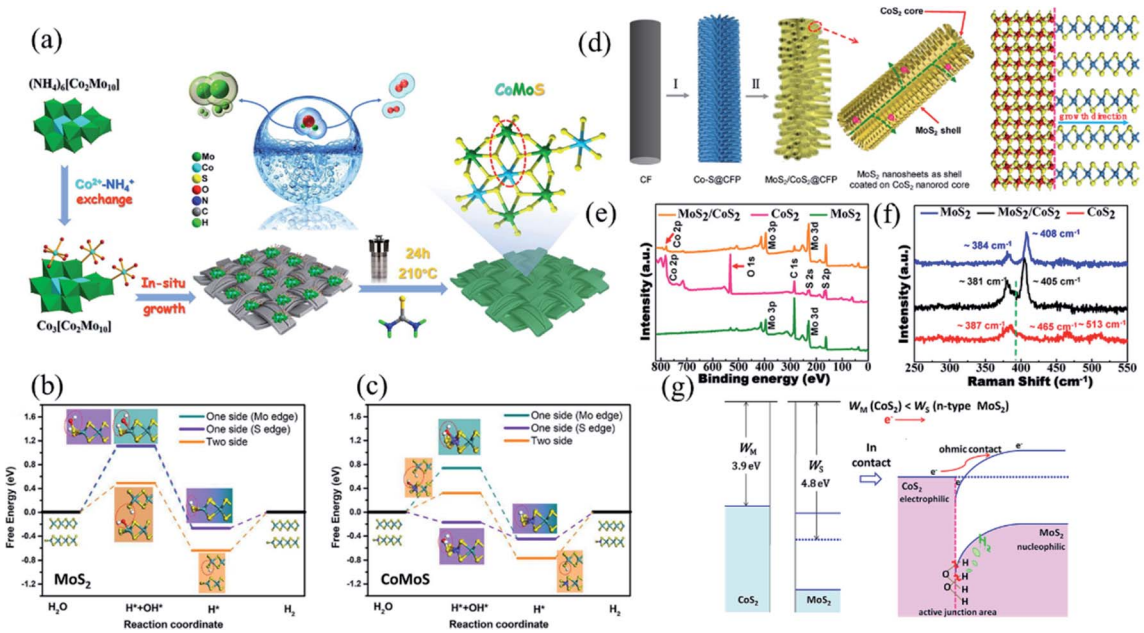

Fig. 9 (a) Schematic representation for the preparation of $Co_5Mo_{10}S_x$/CC. (b and c) Gibbs free energy diagrams for alkaline HER on the possible active sites of MoS_2 and CoMoS catalysts. The optimized adsorption surface structures at different stages are shown in the inset. The S, Mo, Co, H, and O atoms are represented by orange, green, blue, white, and red spheres, respectively. Reproduced with permission.[105] Copyright 2020, Elsevier. (d) Brief illustration of the synthetic process and structure of the MoS_2/CoS_2 hybrid and brief illustration of the heteroepitaxy-like growth of MoS_2 on CoS_2, where yellow balls, blue balls, and red balls respectively represent the S, Mo, and Co elements. (e) XPS survey spectra of MoS_2/CoS_2, CoS_2, and MoS_2. (f) Raman spectra of MoS_2/CoS_2, MoS_2, and CoS_2. (g) Schematic diagram for the band structure of CoS_2 and n-type MoS_2 before contact, and the ohmic contact and the charge transfer between metallic CoS_2 and n-type MoS_2. Reproduced with permission.[106] Copyright 2019, American Chemistry Society.

CoS_2 to MoS_2. After the electron transfer in the MoS_2/CoS_2 heterogeneous interface, the CoS_2 side forms an electrophilic region, while the MoS_2 side forms a nucleophilic region. Due to the difference in electronegativity, for polar water molecules, CoS_2 and MoS_2 will attract negative O and positive H, respectively. This interaction will promote the cleavage of the O–H bond, thereby promoting water splitting. In addition, according to semiconductor physics, if the work function of the metal is

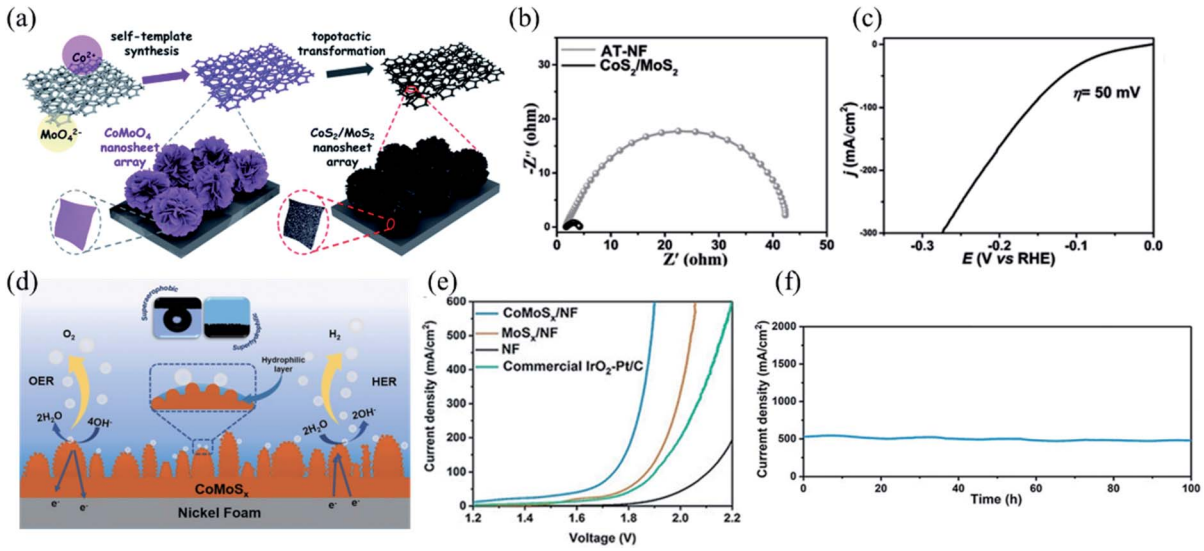

Fig. 10 (a) Schematic illustration of the preparation of $CoMoO_4$ and *in situ* sulfurization to CoS_2/MoS_2. (b) Nyquist plots of acid-treated Ni foam and CoS_2/MoS_2 in 1.0 M KOH. (c) Polarization curves of CoS_2/MoS_2. Reproduced with permission.[110] Copyright 2020, Royal Society of Chemistry. (d) Schematic superhydrophilic/superaerophobic design of the $CoMoS_x$/NF electrocatalysts for overall water splitting. (e) Overall water splitting polarization curves of $CoMoS_x$/NF, MoS_x/NF, IrO_2–Pt/C and pristine NF electrodes at a scan rate of 5 mV s^{-1}, respectively. (f) Catalytic stability of $CoMoS_x$/NF for overall water splitting at 500 mA cm^{-2} for 100 hours. Reproduced with permission.[113] Copyright 2020, Wiley-VCH.

smaller than that of the n-type semiconductor, the metal–semiconductor contact will be an ohmic contact with no obvious junction resistance, so that electrons can be smoothly transferred through the MoS_2/CoS_2 interface (Fig. 9g).

The optimization of the nanostructure can increase the specific surface area and expose more active sites for electrocatalysts.[107–109] Shi *et al.* prepared a flower-like CoS_2/MoS_2 hetero-nanosheet array *via in situ* sulfurization of the $CoMoO_4$ nanosheet array on NF (Fig. 10a).[110] The usage of the $CoMoO_4$ nanosheet array as a precursor enabled the well-maintained 3D network structure with high surface area and excellent conductivity after sulfurization (Fig. 10b). The flower-like structure can not only expose more heterogeneous interfaces, but also facilitate the contact of active sites with the electrolyte. Benefiting from the structural advantages and heterogeneous interface effects, the CoS_2/MoS_2 hetero-nanosheet array showed high catalytic performance for HER, with a low overpotential of 50 mV at a current density of 10 mA cm^{-2} in 1 M KOH (Fig. 10c).

The water splitting reaction is a process of producing gas; if the generated bubbles cannot be released from the electrode in time, the active sites would be blocked and also impede the diffusion of the electrolyte, resulting in the poor contact between the catalyst and electrolyte.[111,112] Compared with non-self-supporting catalysts, self-supporting catalysts more easily achieve surface hydrophilic/hydrophobic engineering.[96] Shan *et al.* reported the preparation of superhydrophilic/superaerophobic amorphous $CoMoS_x$ chalcogel catalysts supported on nickel foam (NF) for overall water splitting (Fig. 10d).[113] The prepared $CoMoS_x$/NF shows superhydrophilicity, which facilitates the penetration of electrolytes, and superhydrophobicity, which promotes the fast release of the evolving gas bubbles. Moreover, the introduction of Co creates abundant active sites and defects. By employing $CoMoS_x$/NF as bifunctional electrocatalysts, the overall water splitting device delivered 500 mA cm^{-2} current density at a low voltage of 1.89 V and without decay in performance for 100 hours (Fig. 10e and f).

Although self-supporting composites exhibit higher catalytic activity, it should be noted that the mass loading of the self-supporting catalysts is much higher that of the non-self-supporting catalysts, and few reports in the literature compared the mass activity of the catalysts. For future investigations, it is better to report the mass activity of the catalysts, rather than simply the area activity for self-supporting catalysts.

5.2 Self-supporting NiS_x–MoS_2 composites

Nickel foam (NF) possesses 3D porous structures and excellent electrical conductivity, which can not only facilitate the good contact between the electrolyte and catalysts, but also reduce the charge transport resistance of the material in the electrochemical reaction.[114,115] In addition, nickel foam can serve as a Ni source in the material preparation process to prepare self-supporting electrocatalysts.[116–118] Wu *et al.* synthesized three-dimensional curved nanosheets of Mo-doped Ni_3S_2 grown on NF through a one-step hydrothermal method.[119] The Mo doping can change the morphology of the catalyst from an upright

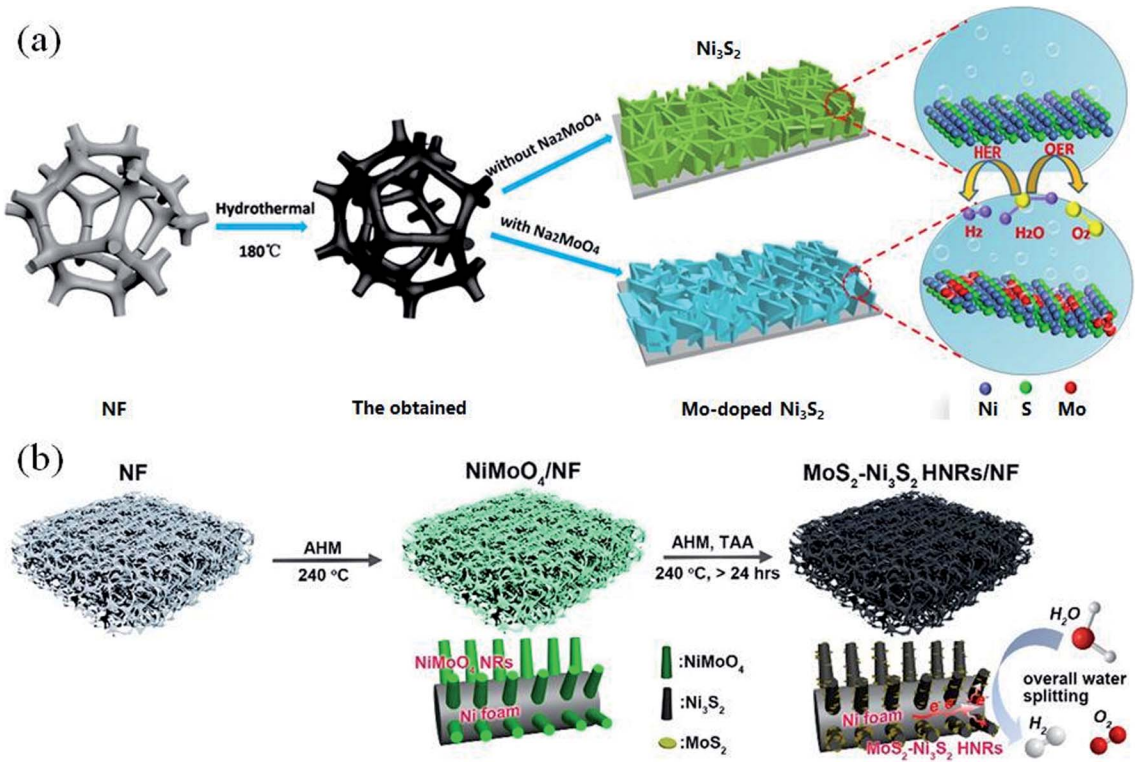

Fig. 11 (a) Illustration of the designed Mo-doped Ni_3S_2 nanosheets.[119] Copyright 2018, Elsevier. (b) Illustration of the fabrication of the heterostructured MoS_2–Ni_3S_2 HNRs/NF composites. Reproduced with permission.[120] Copyright 2017, American Chemistry Society.

rectangular to wavy nanosheet interweave. The curved and patulous morphology could enable more abundant catalytic active sites for OER and HER (Fig. 11a). Yang *et al.* used ammonium molybdate and nickel foam as raw materials to synthesize MoS_2–Ni_3S_2 heterogeneous rods supported on nickel foam through the one-pot hydrothermal method (Fig. 11b).[120] MoS_2–Ni_3S_2 electrocatalysts displayed superior performance for HER and OER, which achieved low overpotentials of 98 and 290 mV at 10 mA cm^{-2}, respectively. As for the overall water splitting, a cell voltage of only 1.50 V is required for a j of 10 mA cm^{-2}. Such excellent activity can be ascribed to the good exposure of the heterogeneous interface in the hierarchical nanostructure, which is conducive to the chemical adsorption of H- and O-containing intermediates, and the facilitated electron transport along 1D Ni_3S_2 that is anchored on the NF substrate. Zhang *et al.* investigated the interface engineering of MoS_2/Ni_3S_2 heterostructures supported on nickel foam.[121] The inner Ni_3S_2 nanoparticles were modified by MoS_2 nanosheets on their surfaces to result in abundant MoS_2/Ni_3S_2 hetero interfaces. In alkaline medium, MoS_2/Ni_3S_2 exhibits excellent HER and OER catalytic activity. When MoS_2/Ni_3S_2 is used as a bifunctional catalyst, an alkali electrolyzer delivers a current density of 10 mA cm^{-2} at a very low cell voltage of 1.56 V. The author calculated the chemisorption free energies of hydrogen (ΔG_H) and hydroxide (ΔG_{OH}) on the (101) surface of Ni_3S_2 and the (002) surface of MoS_2 by density functional theory. It was found that compared with the H adsorption energy of the (101) plane of Ni_3S_2 and the (002) plane of MoS_2, H was more easily adsorbed on the Mo–S edge of the Ni-doped MoS_2 model, which has the lowest H chemisorption free energy (3.17 eV). Similarly, due to the lowest OH chemisorption free energy (−2.92 eV), oxygen-containing intermediates tend to adsorb on the under-coordinated Ni sites of the Mo-doped Ni_3S_2 model. In summary, the MoS_2/Ni_3S_2 heterogeneous interface accelerates the decomposition of H_2O in alkaline media by reducing the adsorption free energy for intermediate product, and finally, the HER and OER activities of the bimetallic sulfide are enhanced.

The bimetallic sulfide MoS_2/NiS_x heterogeneous interface can adjust the intermediate species' adsorption energy. However, due to the greater electronegativity of S, the strong interaction between S and the adsorbed H hinders the Tafel/Heyrovsky step in HER. Introducing non-metallic anions to adjust the electron density and catalytic active centers of the bimetallic sulfides is a suitable strategy to improve the Tafel/Heyrovsky step of HER.[122–124] Yang *et al.* synthesized nitrogen anion-decorated NiS/MoS_2 heterostructures for HER. The interface between MoS_2 and NiS can be clearly seen from the TEM image, indicating the formation of unique NiS/MoS_2 hetero-interfaces. Through first-principles density functional theory calculations,[125] the author first calculated the effect of N doping on the electron density of N–NiS. As shown in Fig. 12a, the density of states of N–NiS and NiS are continuous at the Fermi level, indicating the intrinsic metallic properties of N–NiS after the introduction of N atoms. Compared with NiS (−4.64 eV), the H_2O dissociation free energy of N–NiS (−6.97 eV) is lower. Similarly, compared to MoS_2 (0.48 eV), the H_2O dissociation free energy of N–MoS_2 (−0.06 eV) is also much smaller (Fig. 12b), proving that the introduction of non-metal atoms can enhance the electrocatalytic performance. By calculating the charge density difference, it is shown that the charge polarization of N–NiS and N–MoS_2 causes a strong charge redistribution at the heterogeneous interface (Fig. 12c), and the ΔG_H of the N–NiS/MoS_2 heterojunction is close to 0, which makes it exhibit better HER catalytic performance. In addition, N–NiS/MoS_2 exhibits very good stability without a noticeable decrease in the current density after 20 h chronoamperometry measurement, and the morphology of the catalysts is well maintained (Fig. 12d).

The H_2O adsorption on the surface of the catalysts is the first step in the water splitting process, and this step is affected by the wettability of the material surface. Hydrophilic catalysts can adsorb water molecules well. The better the hydrophilicity, the better the compatibility with water; an improved wettability can strongly enhance the water splitting performance.[126,127] Li *et al.* synthesized a superhydrophilic porous MoS_2/Ni_3S_2 catalyst grown on nickel foam (p-MoS_2/Ni_3S_2/NF) through electrodeposition and the solvothermal reaction.[128] The author proved the hydrophilicity of the materials and the relationship between hydrophilicity and pore structure through the contact angle test. As shown in Fig. 12e–i, Ni_3S_2/NF, MoS_2/NF and NF all exhibit hydrophobicity, whose contact angle is greater than 90°. Conversely, the contact angle of nonporous MoS_2/Ni_3S_2/NF is 70°, and a water droplet can be quickly absorbed by MoS_2/Ni_3S_2/NF within 0.5 s. As for p-MoS_2/Ni_3S_2/NF, water droplets are completely adsorbed as soon as they touch the surface of the catalyst, demonstrating its superhydrophilicity. During the reaction, a large number of O_2 and H_2 bubbles gathered in the non-porous MoS_2/Ni_3S_2/NF. In contrast, no large bubbles were observed on the p-MoS_2/Ni_3S_2/NF catalyst. This was probably due to the quick adsorption of water that promoted the squeeze of gas bubbles (Fig. 12j and k).

5.3 Self-supporting MoS_2-based trimetallic sulfides composites

MoS_2 possesses rich unsaturated S boundaries. Experiments and theoretical calculations have proved that MoS_2 is an excellent HER catalyst.[129] However, its OER performance under alkaline conditions is not satisfactory, which limits the use of MoS_2 as a bifunctional catalyst for water splitting.[130] In order to solve this problem, a good strategy is to integrate MoS_2 with high active OER catalysts to adjust the electronic structure of the heterogeneous interfaces and accelerate the water dissociation.[131] In recent years, it has been proved that NiFe-based composites are excellent OER catalysts.[132,133] Therefore, integrating NiFe-based composites with MoS_2 can achieved high performance bifunctional catalysts for overall water splitting.

Using FeNi foam as a substrate for the growth of MoS_2, Wu *et al.* synthesized $MoS_2/Fe_5Ni_4S_8$ heterostructures and investigated their performance for water splitting. The $Fe_5Ni_4S_8$ (FNS) is *in situ* grown at the interface during the synthesis of MoS_2.[134] XPS measurements showed that the Mo $3d_{5/2}$ and $3d_{3/2}$ feature peaks shifted negatively, indicating the strong electronic interactions between FNS and MoS_2. The synthesized MoS_2/FNS/

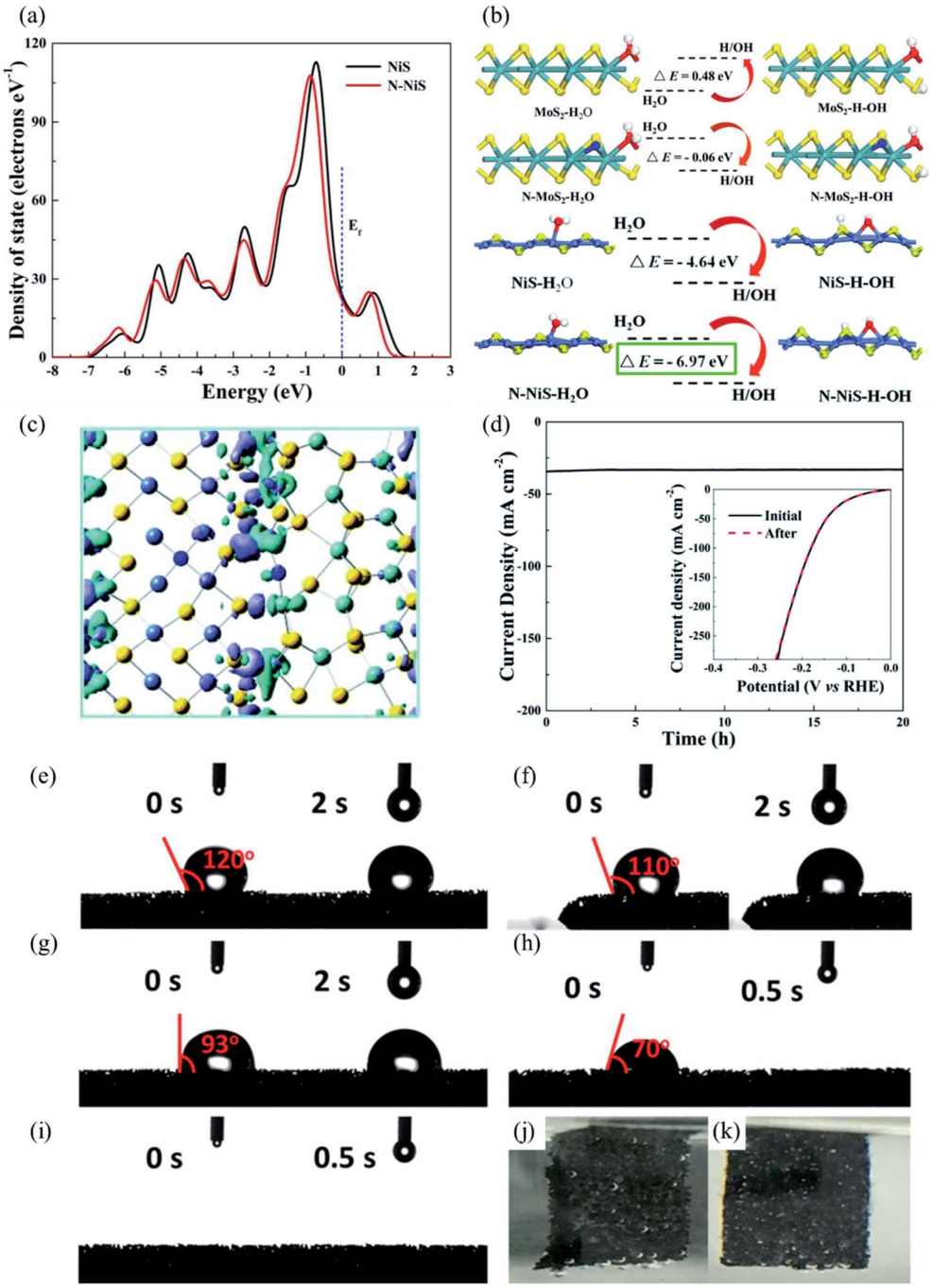

Fig. 12 (a) Calculated density of states for NiS and N–NiS. The Fermi level is set at 0 eV. (b) Adsorbed H_2O dissociation configuration on the surfaces of the MoS_2 (002) facet, N–MoS_2 (002) facet, NiS (100) facet and N–NiS (100) facet, as well as the corresponding dissociation energies in alkaline solution. Yellow, dark blue, green, light blue, red and white balls represent the S, Ni, Mo, N, O and H atoms, respectively. (c) The charge density difference in the heterostructures of N–NiS/MoS_2. The purple and blue isosurfaces represent the charge accumulation and depletion in the space, respectively. (d) Current density *versus* time (*i*–*t*) curves of N–NiS/MoS_2 recorded for 20 h at 30 mA cm^{-2}. Inset: polarization curves before and after the *i*–*t* test.[125] Copyright 2019, Royal Society of Chemistry. (e–i) Contact angle of the as-prepared catalysts. The calculated hydrogen adsorption free energy changes for NiS, N–NiS, MoS_2, and N–MoS_2. Reproduced with permission. (e–i) Contact angle of the as-prepared catalysts: (e) NF, (f) MoS_2/NF, (g) Ni_3S_2/NF, (h) MoS_2/Ni_3S_2/NF, and (i) p-MoS_2/Ni_3S_2/NF. (j and k) Picture of (j) MoS_2/Ni_3S_2/NF and (k) p-MoS_2/Ni_3S_2/NF during the reaction under the same electrocatalytic condition. Reproduced with permission.[128] Copyright 2018, American Chemistry Society.

FeNi foam achieved a current density of 10 mA cm^{-2} at very low overpotentials of 120 and 204 mV for HER and OER, respectively (Fig. 13a and b). In addition to the high catalytic activity, the MoS_2/FNS/FeNi also possesses higher HER stability than that of Pt/C (72.6% *vs.* 63.2% current retention) and comparable OER stability with IrO_2 (Fig. 13c and d). The author clarified the

influence of the MoS_2/FNS heterogeneous interface on the enhancement for HER and OER through density functional theory calculations. First of all, for HER, the author found that compared to the H adsorption energy (−0.649 eV) on the (103) plane of MoS_2, the H adsorption energy on the (103) plane at the S edge sites of FeNi–MoS_2 is −1.575 eV, which leads to the tendency of the H protons to be adsorbed on the S boundary sites of the MoS_2/FNS heterogeneous interface, thereby enhancing the HER performance. Secondly, for OER, the OH chemisorption energy of the uncoordinated Fe sites on Mo–Fe_9S_8 is −2.921 eV, which is lower than that of Fe_9S_8 (−0.940 eV). Similarly, for Mo–Ni_9S_8, the OH chemisorption energy at the uncoordinated Ni site is −2.438 eV, which is lower than that of Ni_9S_8 (−1.839 eV). These results prove that the MoS_2/FNS heterogeneous interface facilitates the absorption of H atoms and OH groups, consequently enhancing the performances for HER and OER. As shown in Fig. 13e, the author gives the mechanisms of HER and OER on MoS_2/FNS.

Liu *et al.* synthesized (Ni, Fe)S_2@MoS_2 heterostructures for HER and OER through a two-step method. First, NiFe–LDH nanosheets supported on carbon fiber paper were synthesized by hydrothermal method. Then, thioacetamide and sodium molybdate were added to generate (Ni, Fe)S_2 nano-boxes covered with layers of MoS_2 nanosheets (Fig. 13f).[135] The author recorded the formation process of S–H_{ads} through *in situ* Raman spectra and revealed that the heterogeneous interface formed between trimetallic sulfides is favored by the adsorption of H and the formation of S–H_{ads}, therefore boosting its overall water splitting performance (Fig. 13g and h). Using (Ni, Fe)S_2@MoS_2 to assemble a water splitting device, the electrolyzer only needs 1.56 V to achieve a current density of 10 mA cm^{-2} (Fig. 13i). In addition, by adjusting the interface between (Ni, Fe)S_2@MoS_2 and the electrolyte through introducing S ions into the electrolyte, the leaching of atomic S in the sulfides can be effectively relieved, and the stability of the catalysts can be significantly improved (Fig. 13j).

NiCo-based composites also showed excellent OER activity.[136,137] Yang *et al.* synthesized a hierarchical co-assembly of interacting MoS_2 and Co_9S_8 nanosheets attached on Ni_3S_2 nanorod arrays, which are supported on nickel foam by hydrothermal method using nickel foam as the substrate and Ni source, thiourea as the S source, and cobalt sulfate and sodium molybdate as the Co and Mo sources, respectively (Fig. 14a).[138] When the ratio of Mo : Co is 1 : 3, the obtained CoMoNiS–NF-31 shows that Co_9S_8 and MoS_2 nanosheets are directly grown on Ni_3S_2 nanorods, and there is no excess nanosheet to form an aggregation. This structure can make full use of the active centers. In addition, Co_9S_8, MoS_2 and Ni_3S_2 completely cover the original NF surface, which improves the durability of the 3D frame structure, making CoMoNiS–NF-31 display an

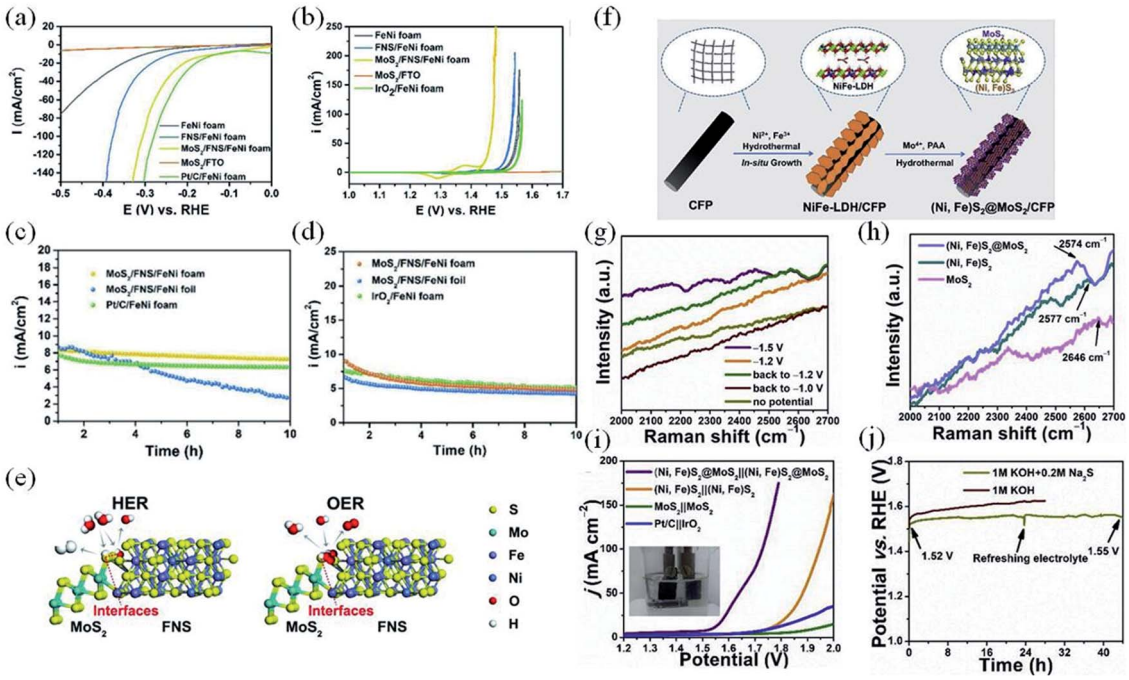

Fig. 13 (a and b) Polarization curves of the MoS_2/FNS/FeNi foam, FNS/FeNi foam, FeNi foam, and MoS_2/FTO in 1 M KOH for HER and OER, respectively. (c) Chemisorption models and corresponding adsorption energy of H and OH on the surfaces of MoS_2, Fe_9S_8, Ni_9S_8, MoS_2/FNS (Fe, Ni–MoS_2 model), MoS_2/Fe_9S_8 (Mo–Fe_9S_8 model), and MoS_2/Ni_9S_8 (Mo–Ni_9S_8 model) heterostructures. (d) Current density *versus* time (*i*–*t*) curves of the MoS_2/FNS/FeNi foam and MoS_2/FNS/FeNi foil for HER and OER. (e) Illustration for the fabrication of (Ni, Fe)S_2@MoS_2 heterostructures. Reproduced with permission.[134] Copyright 2018, Wiley-VCH. (f) Illustration for the fabrication of (Ni, Fe)S_2@MoS_2 heterostructures. (g) *In situ* Raman spectra of (Ni, Fe)S_2@MoS_2 at different potentials at range of 2000–2700 cm^{-1}, (h) *In situ* Raman spectra at 2000–2700 cm^{-1} for (Ni, Fe)S_2@MoS_2, (Ni, Fe)S_2 and MoS_2. (i) LSV curves of two-electrode cell assembled by different materials (inset: the optical image of two-electrode setup). (j) Stability test of different electrolytes for (Ni, Fe)S_2@MoS_2. Reproduced with permission.[135] Copyright 2019, Elsevier.

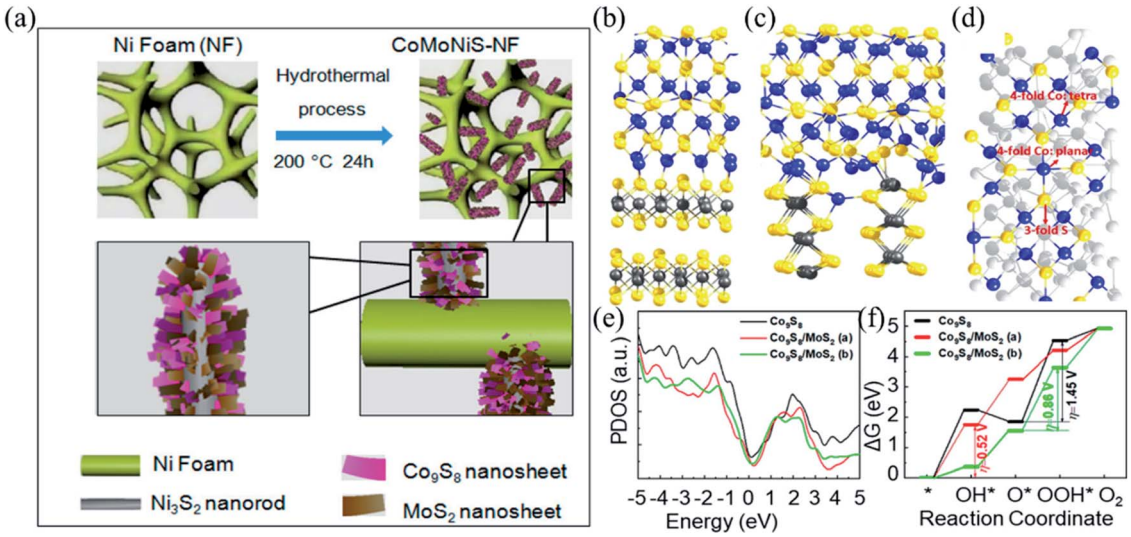

Fig. 14 (a) Schematic illustration of the synthesis and growth of hierarchical CoMoNiS–NF-*xy* composites *via* one-pot hydrothermal method. (b and c) DFT-optimized structures of the MoS_2/Co_9S_8 interfaces: (b) MoS_2 (001) parallel to Co_9S_8 (001) and (c) MoS_2 (001) perpendicular to Co_9S_8 (001). Atom colors: Mo, black; Co, blue; and S, yellow. Co-termination at the interface results in the most stable structure. (d) Top view of the Co_9S_8 (001) surface sites used for DFT calculations of the adsorbed O*, OH*, and OOH* species. (e) Calculated densities of the electronic states for the MoS_2/Co_9S_8 interfaces with Co termination and with Co_9S_8. (f) Gibbs free energy changes for the four steps of OER at 0 V *vs.* standard hydrogen electrode. Reproduced with permission.[138] Copyright 2019, Royal Society of Chemistry.

outstanding balance between the catalytic activity and stability, according to the activity-stability factor. The author investigated the influence of the MoS_2/Co_9S_8 heterogeneous interface on the OER catalytic activity through density functional theory calculations (Fig. 14b–d). The two structures of the MoS_2 layer parallel and perpendicular to the Co-terminated Co_9S_8 interface were chosen to study the charge transfer in OER. The results show that when Co_9S_8 is combined with MoS_2, the Fermi level will decrease, and electrons will be transferred from Co_9S_8 to MoS_2 through sulfur atoms at the Co-terminated interface (Fig. 14e). By calculating the O*, OH* and OOH* intermediates at different surface positions, the author estimates that the Gibbs free energy of the four electrochemical reaction steps occurred in OER on the Co_9S_8 surface in the Co_9S_8/MoS_2 (Fig. 14f). It was found that when Co_9S_8 transfers electrons to MoS_2, the binding energy of the OER adsorption species changes and the overpotentials decrease, indicating that the OER activity of Co_9S_8 strongly depends on the existence of heterogeneous interfaces with other transition metal sulfides. The CoMoNiS–NF-31 demonstrates the best electrocatalytic activity, giving ultralow overpotentials (113, 103, and 117 mV for HER and 166, 228, and 405 mV for OER) to achieve a current density of 10 mA cm^{-2} in alkaline, acidic, and neutral electrolytes, respectively.

Mo and W have similar electronic structures. According to theoretical studies, the introduction of foreign metal atoms with similar atomic radius and electronic configuration will inevitably lead to the imbalance of the local Coulomb force, and the derivative disturbance from the rearrangement of atoms will generate additional exposed edge sites. Therefore, the introduction of W will cause changes in the electronic structure of Mo-based materials and improve the overall conductivity and catalytic activity. Zheng *et al.* synthesized few-layered $Mo_{(1-x)}W_xS_2$ hollow nanospheres-modified Ni_3S_2 heterostructures through the one-step hydrothermal reaction.[139] The layered hollow structure of $Mo_{(1-x)}W_xS_2$ not only exposes a large number of accessible active sites, but also is conducive to the mass and charge transfer during the reaction. The doping of W establishes a ternary sulfide coupling interface, which enables a strong electronic interaction between $Mo_{(1-x)}W_xS_2$ and Ni_3S_2 to optimize the electronic structure at the interface and improve the conductivity of the ternary sulfide. As a result, the $Mo_{(1-x)}W_xS_2@Ni_3S_2$ heterostructure exhibited good bifunctional performance, with a cell voltage of 1.62 V to deliver a current density of 10 mA cm^{-2} for water splitting.

6. Summary and outlook

The development of high-efficiency and low-cost HER/OER catalysts is critical to the application of water splitting devices. MoS_2 has been proved to possess excellent HER intrinsic activity due to its abundant unsaturated S boundary by theory and experiment. In order to optimize the HER performance of MoS_2-based catalysts and enhance their OER performance, constructing multiple heterogeneous interfaces is a good and effective strategy. In this review, from two major aspects of non-self-supporting catalysts and self-supporting catalysts, we reviewed the recent progress on the construction of heterogeneous interfaces between MoS_2 and other transitional metal sulfides for water splitting. The preparation process and structural characteristics of each material are introduced, the enhancement effect of the heterogeneous interface on the HER/OER performances of the catalysts are addressed, and the possible catalysis mechanism are discussed

to give readers a deep comprehension of the advantages of this kind of electrocatalyst.

As a branch in the development of water splitting catalysts, MoS_2 based multi-metal sulfides have received a lot of attention in recent years and outstanding performances were achieved. However, we could not ignore some of the shortcomings and challenges in the current research, and some of the more critical points should be addressed in future investigations.

(i) Insufficient understanding of the reaction mechanism. Although great progress has been made in developing MoS_2-transitional metal sulfides for water-slitting, the catalytic mechanism is still not clear. Nowadays, the most frequently proposed mechanism is the electron transfer between the different metal sulfides that promotes the H or OH adsorption. However, it should be noted that the desorption step of the products is still very important and the related investigated is rare. In addition, the interaction between the heterogeneous interfaces composed of multiple metals needs to be studied systematically to clearly explain how the so-called "synergistic effect" occurs. Moreover, the metal sulfides are an unstable species, especially under electrochemical oxidization conditions, like the metal phosphides and metal selenides. It is proposed that the metal sulfides will transform into metal (hydro)oxides during the reaction process. However, this is ignored in most of the current literature. Therefore, it is urgent to clarify the real active sites and catalytic mechanism. The use of theoretical calculations and *in situ* technology, coupled with the proof of experimental results, will help research studies in better understanding the mystery of water splitting.

(ii) Systematic research is still lacking. Although many of the metal sulfides have been composited with MoS_2 to investigate the performance of the catalysts, a systematic approach is still lacking nowadays. It is well known that there are many crystalline phases for metal sulfides. For example, CoS, CoS_2, Co_3S_4 and Co_9S_8 are common cobalt sulfides and each of them have been composited with MoS_2, and many catalytic data have been collected. However, it should be noted that the electrocatalysts are in various nanostructures, morphologies, crystallinity, and combination mode with MoS_2. Therefore, we could not compare the performance of the catalysts effectively. One of the major difficulties is that the synthesis of various crystalline-phased metal sulfide–MoS_2 composites with the same nanostructures, morphologies, crystallinity is very challenging. In addition, optimizing the ratio of the metal sulfides and MoS_2 in the heterostructure to achieve the best performance is rare, and lots of work should be done to reveal this. Theoretical calculations may be a good strategy to selectively predict the best catalysts for saving time and labor costs.

(iii) More effective and cost-effective supports should be developed. For self-supporting catalysts, nowadays, the most widely utilized supports are Ni foam and carbon cloth. For the use of Ni foam supports, it is inevitable to introduce NiS_x in the catalysts, which not only limit the diversity of the composites, but also bring difficulties in understanding the catalytic mechanism due to the complicated compositions and interfaces of the catalysts. The utilization of carbon as supports could avoid the above issues. However, the high cost of carbon cloth hinders its widespread applications. Therefore, it is still urgent to develop more diverse and cost-effective supports, especially the supports that involve easy-to-implement hydrophilic/hydrophobic engineering to achieve improved catalytic performance based on the advantaged of the substrates.

(iv) The evaluation criteria need to be improved. At present, most of the evaluations for water splitting catalysts are based on the overpotential under 10 mV cm_{geo}^{-2}. Although this standard can roughly distinguish the performance of the catalyst, the area of the working electrode is not equivalent to the area used by the catalyst. Moreover, this evaluation standard is based on different loadings and various test conditions. It is also difficult to compare the performance of the catalysts based on different literature studies. Therefore, standard testing conditions should be established for better comparison of the performance of catalysts, and at least the authors should clearly describe the test conditions in their manuscripts. Furthermore, nowadays most of the literature studies are focused on evaluating the performance of the catalysts in aqueous condition in the single cell, where the mass transportation is limited and the oxygen and hydrogen is mixed. For practical application, a membrane-based electrolyzer would be more efficient and the related investigation is very rare. Therefore, it is more significant to construct a membrane-based electrolyzer to evaluate the activity and practical application of the catalysts in the future.

(v) The nanostructures of the catalysts need to be optimized. The structure of the catalyst has a great influence on its electrocatalytic performance. On the one hand, a larger specific surface area means more active sites. On the other hand, an excellent structure can optimize the mass transfer capacity during the catalytic process, leading to better kinetic performances. The water splitting is a process of producing gas, which makes the requirement for the mass transfer capacity of the catalyst higher. However, at the current stage, it is still challenging to effectively construct porous structures, especially hierarchical structures that possess both high specific surface area and fast mass transport. Therefore, more effective strategies should be developed to construct superior nanostructure catalysts for water splitting.

Conflicts of interest

There are no conflicts to declare.

Acknowledgements

This work has been financially supported by the National Natural Science Foundation of China (No. 51972293, 51772039, 21902189 and 21901264), Key Scientific Research Projects of Universities in Henan Province (21A150062) and Young Backbone Teacher of Zhongyuan University of Technology.

Notes and references

1 M. Simoes, S. Baranton and C. Coutanceau, *Appl. Catal. B Environ.*, 2010, **93**, 354–362.

2 H. Wen, G.-X. Cao, M.-H. Chen, Y.-P. Qiu, L.-Y. Gan and P. Wang, *Appl. Catal. B Environ.*, 2020, **268**, 118388.
3 T. Q. Guo, Y. Z. Song, Z. T. Sun, Y. H. Wu, Y. Xia, Y. Y. Li, J. H. Sun, K. Jiang, S. X. Dou and J. Y. Sun, *J. Energy Chem.*, 2020, **42**, 34–42.
4 C. C. Liu, T. Gong, J. Zhang, X. R. Zheng, J. Mao, H. Liu, Y. Li and Q. Y. Hao, *Appl. Catal. B Environ.*, 2020, **262**, 118245.
5 F. Safari and I. Dincer, *Energy Convers. Manag.*, 2020, **205**, 112182.
6 D. Zheng, J. Li, S. Ci, P. Cai, Y. Ding, M. Zhang and Z. Wen, *Appl. Catal. B Environ.*, 2020, **277**, 119178.
7 Y. Zhao, N. Jia, X.-R. Wu, F.-M. Li, P. Chen, P.-J. Jin, S. Yin and Y. Chen, *Appl. Catal. B Environ.*, 2020, **270**, 118880.
8 C. L. Hu, L. Zhang and J. L. Gong, *Energy Environ. Sci.*, 2019, **12**, 2620–2645.
9 M. Sangareswari and M. M. Sundaram, *Appl. Water Sci.*, 2017, **7**, 1781–1790.
10 G. Q. Zhao, K. Rui, S. X. Dou and W. P. Sun, *Adv. Funct. Mater.*, 2018, **28**, 1803291.
11 J. Zhu, L. S. Hu, P. X. Zhao, L. Y. S. Lee and K. Y. Wong, *Chem. Rev.*, 2020, **120**, 851–918.
12 L. Xu, Y. Q. Zou, Z. H. Xiao and S. Y. Wang, *J. Energy Chem.*, 2019, **35**, 24–29.
13 A. Muthurasu, V. Maruthapandian and H. Y. Kim, *Appl. Catal. B Environ.*, 2019, **248**, 202–210.
14 Z. P. Lin, B. Lin, Z. P. Wang, S. G. Chen, C. W. Wang, M. Y. Dong, Q. Gao, Q. Shao, T. Ding, H. Liu, S. D. Wu and Z. H. Guo, *ChemCatChem*, 2019, **11**, 2217–2222.
15 J. D. Wu, D. P. Wang, S. Wan, H. L. Liu, C. Wang and X. Wang, *Small*, 2020, **16**, 1900550.
16 Z. Li, Z. Z. Jiang, W. Y. Zhu, C. C. He, P. Wang, X. Wang, T. X. Li and L. Tian, *Appl. Surf. Sci.*, 2020, **504**, 144368.
17 P. Zhang, X. F. Lu, J. W. Nai, S. Q. Zang and X. W. Lou, *Adv. Sci.*, 2019, **6**, 1900576.
18 Z. P. Liu, L. Zhao, Y. H. Liu, Z. C. Gao, S. S. Yuan, X. T. Li, N. Li and S. D. Miao, *Appl. Catal. B Environ.*, 2019, **246**, 296–302.
19 C. Wang, J. Z. Huang, J. Y. Chen, Z. X. Xi and X. L. Deng, *Front. Chem.*, 2019, **7**, 118435.
20 F. Yu, L. Yu, I. K. Mishra, Y. Yu, Z. F. Ren and H. Q. Zhou, *Mater. Today Phys.*, 2018, **7**, 121–138.
21 T. Yoon and K. S. Kim, *Adv. Funct. Mater.*, 2016, **26**, 7386–7393.
22 C. Wang, X. Shao, J. Pan, J. Hu and X. Xu, *Appl. Catal. B Environ.*, 2020, **268**, 118435.
23 X. Xin, Y. Song, S. Guo, Y. Zhang, B. Wang, J. Yu and X. Li, *Appl. Catal. B Environ.*, 2020, **269**, 118773.
24 Q. Qin, L. Chen, T. Wei and X. Liu, *Small*, 2019, **15**, 1803639.
25 H. Xu, Y. Jiao, S. Li, H. Meng, J. Wu, X. Shi, Z. Du, R. Wang and G. Tian, *Int. J. Hydrogen Energy*, 2020, **45**, 13149–13162.
26 X. Liu, P. Wang, Q. Zhang, B. Huang, Z. Wang, Y. Liu, Z. Zheng, Y. Dai, X. Qin and X. Zhang, *Appl. Surf. Sci.*, 2018, **459**, 422–429.
27 X. Wang, J. Wang, X. Zhang, Q. Tian, M. Liu, N. Cai, Y. Xue, W. Chen, W. Li and F. Yu, *ChemCatChem*, 2019, **11**, 1354–1361.
28 Z. Liu, L. Zhao, Y. Liu, Z. Gao, S. Yuan, X. Li, N. Li and S. Miao, *Appl. Catal. B Environ.*, 2019, **246**, 296–302.
29 S. Anantharaj, S. R. Ede, K. Karthick, S. Sam Sankar, K. Sangeetha, P. E. Karthik and S. Kundu, *Energy Environ. Sci.*, 2018, **11**, 744–771.
30 P. Wang, Y. Sheng, F. Wang and H. Yu, *Appl. Catal. B Environ.*, 2018, **220**, 561–569.
31 Y. Jiao, Y. Zheng, M. T. Jaroniec and S. Z. Qiao, *Chem. Soc. Rev.*, 2015, **44**, 2060–2086.
32 M. Hamdani, R. N. Singh and P. Chartier, *Int. J. Electrochem. Sci.*, 2010, **5**, 556–577.
33 G. Wu, A. Santandreu, W. Kellogg, S. Gupta, O. Ogoke, H. G. Zhang, H. L. Wang and L. M. Dai, *Nano Energy*, 2016, **29**, 83–110.
34 X. M. Li, X. G. Hao, A. Abudula and G. Q. Guan, *J. Mater. Chem. A*, 2016, **4**, 11973–12000.
35 J. H. Wang, W. Cui, Q. Liu, Z. C. Xing, A. M. Asiri and X. P. Sun, *Adv. Mater.*, 2016, **28**, 215–230.
36 S. Anantharaj, S. R. Ede, K. Sakthikumar, K. Karthick, S. Mishra and S. Kundu, *ACS Catal.*, 2016, **6**, 8069–8097.
37 Q. Ding, B. Song, P. Xu and S. Jin, *Chem*, 2016, **1**, 699–726.
38 M. S. Balogun, Y. C. Huang, W. T. Qiu, H. Yang, H. B. Ji and Y. X. Tong, *Mater. Today*, 2017, **20**, 425–451.
39 N. K. Chaudhari, H. Jin, B. Kim and K. Lee, *Nanoscale*, 2017, **9**, 12231–12247.
40 J. Bai, T. Meng, D. Guo, S. Wang, B. Mao and M. Cao, *ACS Appl. Mater. Interfaces*, 2018, **10**, 1678–1689.
41 Y. Wang, W. Kang, D. Cao, M. Zhang, Z. Kang, Z. Xiao, R. Wang and D. Sun, *J. Mater. Chem. A*, 2018, **6**, 4776–4782.
42 X. Wang, J. Wang, X. Zhang, Q. Tian, M. Liu, N. Cai, Y. Xue, W. Chen, W. Li and F. Yu, *ChemCatChem*, 2019, **11**, 1354–1361.
43 Y. Liu, S. Jiang, S. Li, L. Zhou, Z. Li, J. Li and M. Shao, *Appl. Catal., B*, 2019, **247**, 107–114.
44 F. Du, L. Shi, Y. Zhang, T. Li, J. Wang, G. Wen, A. Alsaedi, T. Hayat, Y. Zhou and Z. Zou, *Appl. Catal., B*, 2019, **253**, 246–252.
45 S. Deng, Y. Zhong, Y. Zeng, Y. Wang, X. Wang, X. Lu, X. Xia and J. Tu, *Adv. Sci.*, 2018, **5**, 1700772.
46 M. Ramos, G. Berhault, D. A. Ferrer, B. Torres and R. R. Chianelli, *Catal. Sci. Technol.*, 2012, **2**, 164–178.
47 H. Zhu, J. Zhang, R. Yanzhang, M. Du, Q. Wang, G. Gao, J. Wu, G. Wu, M. Zhang, B. Liu, J. Yao and X. Zhang, *Adv. Mater.*, 2015, **27**, 4752–4759.
48 S. H. Yang, S.-K. Park, J. K. Kim and Y. C. Kang, *J. Mater. Chem. A*, 2019, **7**, 13751–13761.
49 Y. Li, X. Wu, H. Zhang and J. Zhang, *Nanoscale*, 2019, **11**, 15763–15769.
50 V. Ganesan, S. Lim and J. Kim, *Chem.–Asian J.*, 2018, **13**, 413–420.
51 H. Li, X. Qian, C. Xu, S. Huang, C. Zhu, X. Jiang, L. Shao and L. Hou, *ACS Appl. Mater. Interfaces*, 2017, **9**, 28394–28405.
52 Y. Guo, J. Tang, H. Qian, Z. Wang and Y. Yamauchi, *Chem. Mater.*, 2017, **29**, 5566–5573.
53 X. Lei, K. Yu, H. Li and Z. Zhu, *Electrochim. Acta*, 2018, **269**, 262–273.

54 J. Zhang, J. Fang, J. Han, T. Yan, L. Shi and D. Zhang, *J. Mater. Chem. A*, 2018, **6**, 15245–15252.
55 T.-T. Chen, R. Wang, L.-K. Li, Z.-J. Li and S.-Q. Zang, *J. Energy Chem.*, 2020, **44**, 90–96.
56 Y. Zhu, L. Song, N. Song, M. Li, C. Wang and X. Lu, *ACS Sustainable Chem. Eng.*, 2019, **7**, 2899–2905.
57 J. Sun, Z. Huang, T. Huang, X. Wang, X. Wang, P. Yu, C. Zong, F. Dai and D. Sun, *ACS Appl. Energy Mater.*, 2019, **2**, 7504–7511.
58 Y. Guo, T. Park, J. W. Yi, J. Henzie, J. Kim, Z. Wang, B. Jiang, Y. Bando, Y. Sugahara, J. Tang and Y. Yamauchi, *Adv. Mater.*, 2019, **31**, 1807134.
59 Z. Chen, X. Duan, W. Wei, S. Wang and B.-J. Ni, *J. Mater. Chem. A*, 2019, **7**, 14971–15005.
60 X. Zheng, X. Han, Y. Zhang, J. Wang, C. Zhong, Y. Deng and W. Hu, *Nanoscale*, 2019, **11**, 5646–5654.
61 J. Li and G. Zheng, *Adv. Sci.*, 2017, **4**, 1600380.
62 L. Zeng, K. Sun, X. Wang, Y. Liu, Y. Pan, Z. Liu, D. Cao, Y. Song, S. Liu and C. Liu, *Nano Energy*, 2018, **51**, 26–36.
63 L. An, J. Feng, Y. Zhang, R. Wang, H. Liu, G.-C. Wang, F. Cheng and P. Xi, *Adv. Funct. Mater.*, 2019, **29**, 1805298.
64 X. Xu, W. Zhong, L. Zhang, G. Liu and Y. Du, *J. Colloid Interface Sci.*, 2019, **556**, 24–32.
65 X.-Y. Zhang, B.-Y. Guo, Q.-W. Chen, B. Dong, J.-Q. Zhang, J.-F. Qin, J.-Y. Xie, M. Yang, L. Wang, Y.-M. Chai and C.-G. Liu, *Int. J. Hydrogen Energy*, 2019, **44**, 14908–14917.
66 J. He, Y. Chen and A. Manthiram, *Adv. Energy Mater.*, 2019, **9**, 1900584.
67 X. Huang, X. Xu, C. Li, D. Wu, D. Cheng and D. Cao, *Adv. Energy Mater.*, 2019, **9**, 1803970.
68 L. Wang, T. Guo, S. Sun, Y. Wang, X. Chen, K. Zhang, D. Zhang, Z. Xue and X. Zhou, *Catal. Lett.*, 2019, **149**, 1197–1210.
69 X. Xu, W. Zhong, L. Wu, Y. Sun, T. Wang, Y. Wang and Y. Du, *Appl. Surf. Sci.*, 2018, **428**, 1046–1055.
70 S. Mao, G. Lu and J. Chen, *Nanoscale*, 2015, **7**, 6924–6943.
71 G. Li, J. Wang, J. Yu, H. Liu, Q. Cao, J. Du, L. Zhao, J. Jia, H. Liu and W. Zhou, *Appl. Catal. B Environ.*, 2020, **261**, 118147.
72 N. Ullah, W. Zhao, X. Lu, C. J. Oluigbo, S. A. Shah, M. Zhang, J. Xie and Y. Xu, *Electrochim. Acta*, 2019, **298**, 163–171.
73 P. Kuang, M. He, H. Zou, J. Yu and K. Fan, *Appl. Catal. B Environ.*, 2019, **254**, 15–25.
74 Y.-H. Li, M.-Y. Yi, J.-Y. Li, Z.-R. Tang and Y.-J. Xu, *Appl. Catal. B Environ.*, 2019, **257**, 117934.
75 L. Zhang, Y. Guo, A. Iqbal, B. Li, D. Gong, W. Liu, K. Iqbal, W. Liu and W. Qin, *Int. J. Hydrogen Energy*, 2018, **43**, 1251–1260.
76 L. Liu, X. Liu and S. Jiao, *J. Colloid Interface Sci.*, 2020, **564**, 77–87.
77 S. Chandrasekaran, L. Yao, L. B. Deng, C. Bowen, Y. Zhang, S. M. Chen, Z. Q. Lin, F. Peng and P. X. Zhang, *Chem. Soc. Rev.*, 2019, **48**, 4178–4280.
78 J. Xu, Y. Zhu, B. S. Yu, C. J. Fang and J. J. Zhang, *Inorg. Chem. Front.*, 2019, **6**, 3510–3517.
79 S. H. Yu, Z. Tang, Y. F. Shao, H. W. Dai, H. Y. Wang, J. X. Yan, H. Pan and D. H. C. Chua, *ACS Appl. Energy Mater.*, 2019, **2**, 5799–5808.
80 S. Liu, S. Li, K. Sekar, R. Li, Y. Zhu, R. Xing, K. Nakata and A. Fujishima, *Int. J. Hydrogen Energy*, 2019, **44**, 25310–25318.
81 Q. Ji, C. Li, J. Wang, J. Niu, Y. Gong, Z. Zhang, Q. Fang, Y. Zhang, J. Shi, L. Liao, X. Wu, L. Gu, Z. Liu and Y. Zhang, *Nano Lett.*, 2017, **17**, 4908–4916.
82 N. S. Mikhaleva, M. A. Visotin, A. A. Kuzubov and Z. I. Popov, *J. Phys. Chem. C*, 2017, **121**, 24179–24184.
83 C. Du, D. Liang, M. Shang, J. Zhang, J. Mao, P. Liu and W. Song, *ACS Sustainable Chem. Eng.*, 2018, **6**, 15471–15479.
84 S. A. Shah, X. P. Shen, M. H. Xie, G. X. Zhu, Z. Y. Ji, H. B. Zhou, K. Q. Xu, X. Y. Yue, A. H. Yuan, J. Zhu and Y. Chen, *Small*, 2019, **15**, 1804545.
85 X. P. Dai, K. L. Du, Z. Z. Li, M. Z. Liu, Y. D. Ma, H. Sun, X. Zhang and Y. Yang, *ACS Appl. Mater. Interfaces*, 2015, **7**, 27242–27253.
86 J. Hu, C. Zhang, P. Yang, J. Xiao, T. Deng, Z. Liu, B. Huang, M. K. H. Leung and S. Yang, *Adv. Funct. Mater.*, 2019, **30**, 1908520.
87 X.-Z. Song, F.-F. Sun, Y.-L. Meng, Z.-W. Wang, Q.-F. Su and Z. Tan, *New J. Chem.*, 2019, **43**, 3601–3608.
88 C. Qin, A. Fan, X. Zhang, S. Wang, X. Yuan and X. Dai, *J. Mater. Chem. A*, 2019, **7**, 27594–27602.
89 C. Si, Y. Wu, Y. Sun, Q. Liu, L. Tang, X. Zhang and J. Guo, *Electrochim. Acta*, 2019, **309**, 116–124.
90 P. S. Adarakatti, M. Mahanthappa, J. P. Hughes, S. J. Rowley-Neale, G. C. Smith, A. S and C. E. Banks, *Int. J. Hydrogen Energy*, 2019, **44**, 16069–16078.
91 C. G. Morales-Guio, L. A. Stern and X. Hu, *Chem. Soc. Rev.*, 2014, **43**, 6555–6569.
92 J. Zhang, Q. Y. Zhang and X. L. Feng, *Adv. Mater.*, 2019, **31**, 1808167.
93 C. Xia, Q. Jiang, C. Zhao, M. N. Hedhili and H. N. Alshareef, *Adv. Mater.*, 2016, **28**, 77–85.
94 H. Sun, X. Xu, Z. Yan, X. Chen, L. Jiao, F. Cheng and J. Chen, *J. Mater. Chem. A*, 2018, **6**, 22062–22069.
95 Z. S. Wang, J. D. Shen, J. Liu, X. J. Xu, Z. B. Liu, R. Z. Hu, L. C. Yang, Y. Z. Feng, Z. C. Shi, L. Z. Ouyang, Y. Yu and M. Zhu, *Adv. Mater.*, 2019, **31**, 1902228.
96 H. M. Sun, Z. H. Yan, F. M. Liu, W. C. Xu, F. Y. Cheng and J. Chen, *Adv. Mater.*, 2020, **32**, 1806326.
97 J. L. Liu, D. D. Zhu, Y. Zheng, A. Vasileff and S. Z. Qiao, *ACS Catal.*, 2018, **8**, 6707–6732.
98 Z. Z. Ma, Q. Zhao, J. P. Li, B. Tang, Z. H. Zhang and X. G. Wang, *Electrochim. Acta*, 2018, **260**, 82–91.
99 M. W. Hu, J. Huang, Q. Z. Li, R. Tu, S. Zhang, M. J. Yang, H. W. Li, T. Goto and L. M. Zhang, *J. Alloys Compd.*, 2020, **827**, 154262.
100 X. L. Zhang, J. J. Shao, W. Huang and X. C. Dong, *Sci. China Mater.*, 2018, **61**, 1143–1153.
101 J. Hou, B. Zhang, Z. Li, S. Cao, Y. Sun, Y. Wu, Z. Gao and L. Sun, *ACS Catal.*, 2018, **8**, 4612–4621.
102 L. Yang, L. Zhang, G. Xu, X. Ma, W. Wang, H. Song and D. Jia, *ACS Sustainable Chem. Eng.*, 2018, **6**, 12961–12968.

103 W. Zhang, X. Zhao, Y. Zhao, J. Zhang, X. Li, L. Fang and L. Li, *ACS Appl. Mater. Interfaces*, 2020, **12**, 10280–10290.
104 P. C. Wang, L. Wan, Y. Q. Lin and B. G. Wang, *Int. J. Hydrogen Energy*, 2019, **44**, 16566–16574.
105 Y. Lu, X. Guo, L. Yang, W. Yang, W. Sun, Y. Tuo, Y. Zhou, S. Wang, Y. Pan, W. Yan, D. Sun and Y. Liu, *Chem. Eng. J.*, 2020, **394**, 124849.
106 N. Huang, Y. Ding, S. Yan, L. Yang, P. Sun, C. Huang and X. Sun, *ACS Appl. Energy Mater.*, 2019, **2**, 6751–6760.
107 C. W. Liang, P. C. Zou, A. Nairan, Y. Q. Zhang, J. X. Liu, K. W. Liu, S. Y. Hu, F. Y. Kang, H. J. Fan and C. Yang, *Energy Environ. Sci.*, 2020, **13**, 86–95.
108 R. Yang, Y. M. Zhou, Y. Y. Xing, D. Li, D. L. Jiang, M. Chen, W. D. Shi and S. Q. Yuan, *Appl. Catal. B Environ.*, 2019, **253**, 131–139.
109 L. L. Huang, D. W. Chen, G. Luo, Y. R. Lu, C. Chen, Y. C. Zou, C. L. Dong, Y. F. Li and S. Y. Wang, *Adv. Mater.*, 2019, **31**, 1901439.
110 M. Shi, Y. Zhang, Y. Zhu, W. Wang, C. Wang, A. Yu, X. Pu and J. Zhai, *RSC Adv.*, 2020, **10**, 8973–8981.
111 H. Li, S. Chen, Y. Zhang, Q. Zhang, X. Jia, Q. Zhang, L. Gu, X. Sun, L. Song and X. Wang, *Nat. Commun.*, 2018, **9**, 2452.
112 X. Sheng, Z. Liu, R. Zeng, L. Chen, X. Feng and L. Jiang, *J. Am. Chem. Soc.*, 2017, **139**, 12402–12405.
113 X. Shan, J. Liu, H. Mu, Y. Xiao, B. Mei, W. Liu, G. Lin, Z. Jiang, L. Wen and L. Jiang, *Angew. Chem., Int. Ed.*, 2020, **59**, 1659–1665.
114 S. X. Yan, S. H. Luo, J. Feng, P. W. Li, R. Guo, Q. Wang, Y. H. Zhang, Y. G. Liu and S. Bao, *Chem. Eng. J.*, 2020, **381**, 122695.
115 P. Tan, B. Chen, H. R. Xu, W. Z. Cai, W. He and M. Ni, *Appl. Catal. B Environ.*, 2019, **241**, 104–112.
116 F. Z. Sun, G. Wang, Y. Q. Ding, C. Wang, B. B. Yuan and Y. Q. Lin, *Adv. Energy Mater.*, 2018, **8**, 1800584.
117 X. Gu, S. Zheng, X. Huang, H. Yuan, J. Li, M. Kundu and X. Wang, *Chem. Commun.*, 2020, **56**, 2471–2474.
118 C. Liang, W. Cao, L. Zhou, P. Yang, X. Zhao, P. Zhao, R. Qiu, L. Yang, Q. s. Huang and D. Astruc, *ChemCatChem*, 2020, **12**, 1647–1652.
119 C. Wu, B. Liu, J. Wang, Y. Su, H. Yan, C. Ng, C. Li and J. Wei, *Appl. Surf. Sci.*, 2018, **441**, 1024–1033.
120 Y. Yang, K. Zhang, H. Lin, X. Li, H. C. Chan, L. Yang and Q. Gao, *ACS Catal.*, 2017, **7**, 2357–2366.
121 J. Zhang, T. Wang, D. Pohl, B. Rellinghaus, R. Dong, S. Liu, X. Zhuang and X. Feng, *Angew. Chem., Int. Ed.*, 2016, **55**, 6702–6707.
122 P. Chen, T. Zhou, M. Chen, Y. Tong, N. Zhang, X. Peng, W. Chu, X. Wu, C. Wu and Y. Xie, *ACS Catal.*, 2017, **7**, 7405–7411.
123 Y. Wu, X. Liu, D. Han, X. Song, L. Shi, Y. Song, S. Niu, Y. Xie, J. Cai, S. Wu, J. Kang, J. Zhou, Z. Chen, X. Zheng, X. Xiao and G. Wang, *Nat. Commun.*, 2018, **9**, 1425.
124 P. Chen, T. Zhou, M. Zhang, Y. Tong, C. Zhong, N. Zhang, L. Zhang, C. Wu and Y. Xie, *Adv. Mater.*, 2017, **29**, 1701584.
125 M. Yang, Y. Jiang, S. Liu, M. Zhang, Q. Guo, W. Shen, R. He, W. Su and M. Li, *Nanoscale*, 2019, **11**, 14016–14023.
126 M. Das, N. Jena, T. Purkait, N. Kamboj, A. De Sarkar and R. S. Dey, *J. Mater. Chem. A*, 2019, **7**, 23989–23999.
127 Q. Hu, G. M. Li, X. F. Liu, B. Zhu, X. Y. Chai, Q. L. Zhang, J. H. Liu and C. X. He, *Angew. Chem., Int. Ed.*, 2019, **58**, 4318–4322.
128 F. Li, D. Zhang, R.-C. Xu, W.-F. Fu and X.-J. Lv, *ACS Appl. Energy Mater.*, 2018, **1**, 3929–3936.
129 L. Li, Z. D. Qin, L. Ries, S. Hong, T. Michel, J. Yang, C. Salameh, M. Bechelany, P. Miele, D. Kaplan, M. Chhowalla and D. Voiry, *ACS Nano*, 2019, **13**, 6824–6834.
130 P. Hu, Z. Jia, H. Che, W. Zhou, N. Liu, F. Li and J. Wang, *J. Power Sources*, 2019, **416**, 95–103.
131 Q. Z. Xiong, Y. Wang, P. F. Liu, L. R. Zheng, G. Z. Wang, H. G. Yang, P. K. Wong, H. M. Zhang and H. J. Zhao, *Adv. Mater.*, 2018, **30**, 1801450.
132 Z. W. Gao, J. Y. Liu, X. M. Chen, X. L. Zheng, J. Mao, H. Liu, T. Ma, L. Li, W. C. Wang and X. W. Du, *Adv. Mater.*, 2019, **31**, 1804769.
133 C. H. Wang, H. C. Yang, Y. J. Zhang and Q. B. Wang, *Angew. Chem., Int. Ed.*, 2019, **58**, 6099–6103.
134 Y. Wu, F. Li, W. Chen, Q. Xiang, Y. Ma, H. Zhu, P. Tao, C. Song, W. Shang, T. Deng and J. Wu, *Adv. Mater.*, 2018, **30**, 1803151.
135 Y. Liu, S. Jiang, S. Li, L. Zhou, Z. Li, J. Li and M. Shao, *Appl. Catal., B*, 2019, **247**, 107–114.
136 H. Xu, Z. X. Shi, Y. X. Tong and G. R. Li, *Adv. Mater.*, 2018, **30**, 1705442.
137 S. H. Bae, J. E. Kim, H. Randriamahazaka, S. Y. Moon, J. Y. Park and I. K. Oh, *Adv. Energy Mater.*, 2017, **7**, 1601492.
138 Y. Yang, H. Yao, Z. Yu, S. M. Islam, H. He, M. Yuan, Y. Yue, K. Xu, W. Hao, G. Sun, H. Li, S. Ma, P. Zapol and M. G. Kanatzidis, *J. Am. Chem. Soc.*, 2019, **141**, 10417–10430.
139 M. Zheng, J. Du, B. Hou and C. L. Xu, *ACS Appl. Mater. Interfaces*, 2017, **9**, 26066–26076.

